

*The following notice is placed here in accordance with Blackwell Publishing's copyright policy.*

The definitive version of this article is available at [www.blackwell-synergy.com](http://www.blackwell-synergy.com).

<http://www.blackwell-synergy.com/doi/abs/10.1111/j.1365-246X.1995.tb06852.x?prevSearch=allfield%3A%28lilly%29>

# Multiwavelet spectral and polarization analyses of seismic records

Jonathan M. Lilly\* and Jeffrey Park

Department of Geology & Geophysics, Yale University, PO Box 208109, New Haven, CT 06520–8109, USA

Accepted 1995 March 23. Received 1995 March 13; in original form 1994 August 14

## SUMMARY

We present an algorithm, based on the wavelet transform and multiple taper spectral analysis, for providing a low-variance spectrum estimate of a non-stationary data process. The ‘multiwavelet’ algorithm uses, within each frequency band, a number of mutually orthogonal Slepian wavelets, optimally concentrated in frequency. The sum of squared wavelet transforms with the Slepian wavelets results in a spectrum estimate that is both low-variance and resistant to broad-band bias. The multiwavelet algorithm is used to estimate the time-varying spectral density matrix  $\mathbf{S}(f, t)$  for two or more time series, in particular for three-component seismic data. Coherent three-component motion is described by motion along a single trajectory, with appropriate projections onto the three component axes. This trajectory is found by applying a singular value decomposition (SVD) to a matrix  $\mathbf{M}(f, t)$  of wavelet transform values. The normalized first singular value of the SVD determines whether a correlation among the three components of the seismogram is statistically significant. Where significant, coherent particle motion is reconstructed by a linear combination of the wavelets with coefficients specified by the first left-singular vector. The polarization of this motion with respect to the coordinate axes is given by the first right-singular vector. Where the wavelets are real-valued, the usefulness of this method is limited to cases in which the three components of the seismic record oscillate in phase with each other, as is often the case for seismic body waves. Elliptical polarization is handled by pairing even and odd Slepian wavelets into complex-valued wavelets, capable of detecting phase shifts between components. We demonstrate the multiwavelet spectrum and polarization estimators on seismic data from a large shallow earthquake in the Solomon Islands, and from the recent deep earthquakes beneath Fiji (1994 March 9) and Bolivia (1994 June 9).

**Key words:** body waves, inverse problem, polarization, spectral analysis, wavelets.

## INTRODUCTION

If one is interested in frequency-dependent, time-limited signals in a seismogram, an estimate  $\hat{\mathcal{S}}(f, t)$  of the time-varying spectrum  $\mathcal{S}(f, t)$  is useful. One way to estimate the time-varying spectrum is by means of discrete Fourier transforms (DFTs) of a sequence of overlapping time intervals that step through a longer time series. However, the choice of an ideal segment duration for a moving-window Fourier transform is often problematic. The window may be too short to encompass long-period signals fully, and may be too long to resolve changes in the behaviour of short-period signals. The nominal frequency resolution of

any spectrum estimate is the Rayleigh frequency  $f_R = 1/T$ . Because  $f_R$  is inversely proportional to the duration  $T$  of the interval analysed, an increase in the time resolution of a time-varying spectrum estimate necessarily results in a loss of frequency resolution. A moving-window DFT has the same time-resolution for all frequencies, or, equivalently, has a uniform resolution in frequency space. This restriction is cumbersome when analysing seismic records, which are a composite of signals of varying durations and frequency content: body waves, surface waves, scattered waves and local resonances.

The ‘time-frequency trade-off’ is one difficulty associated with time-varying spectrum estimates; uncertainty introduced by the stochastic portion of a data series is another. If the data process is stochastic, or is a deterministic signal in noise, the spectrum cannot be determined exactly. A

\*Now at: School of Oceanography, University of Washington, Seattle, WA 98105, USA.

spectrum estimator will tend to fluctuate about some mean value, given many realizations of the process under identical conditions. This fluctuation is the 'variance' of the spectrum estimate, and can be decreased by incorporating information from within a longer time window or a broader frequency band. Hence there is also a trade-off between the uncertainty of a spectrum estimate and its resolution in time and frequency.

The wavelet transform (Daubechies 1992; Press *et al.* 1992) offers an alternative time–frequency trade-off strategy for spectrum estimation, in which the analysed time interval scales inversely with the frequency of interest. The wavelet transform is a promising method for seismic data analysis, as it decomposes a seismogram into a set of band-limited pulses, a paradigm that most seismologists would find agreeable. We have adapted the wavelet transform to improve its spectral leakage properties and to make the trade-off between spectral variance and resolution more explicit, and therefore more susceptible to optimization. We develop a *multiwavelet* algorithm, analogous to the multitaper spectrum estimators of Thomson (1982, 1990), using 'Slepian wavelets', a set of discrete functions whose properties parallel those of the discrete prolate spheroidal sequences. 'Multiwavelet' and 'multitaper' spectrum analyses are closely related, as both seek to minimize spectral leakage in spectrum estimates. Multitaper spectrum estimates use a fixed data window for all oscillation periods. Multiwavelet spectrum estimates scale the data window as a fixed multiple of the period of interest. Multitaper methods use the discrete Fourier transform in computations. Multiwavelet methods use convolutions in computations. (Note that many convolution algorithms, such as the 'conv' routine in Matlab, use the DFT as an intermediate step.)

The optimal statistical properties of Slepian wavelets allow straightforward computation of stable spectrum estimates and other common measures of time- and frequency-dependent behaviour, such as the coherence between multiple time series. This paper uses multiwavelet spectral analysis to detect coherent signals in noisy three-component seismic data, to estimate the polarization of coherent seismic motion, and to reconstruct coherent seismic signals. Used without modification, Slepian wavelets can readily detect and reconstruct rectilinear seismic particle motion, aiding the analysis of body waves. Seismic signals with elliptical particle motion, such as Rayleigh waves and split shear waves, require the combination of Slepian wavelet pairs into the real and imaginary parts of complex-valued wavelets, which are sensitive to coherent, but time-lagged, signals on different components of the seismic record.

### SLEPIAN WAVELETS

Assume that  $\{s_n\}_{n=0}^{N-1}$  represents a discrete sampling (interval  $\Delta t$ ) of a continuous time process. The discrete-time convolution of  $s_n$  with a real-valued function  $\{r_m\}_{m=-M/2+1}^{M/2}$  is

$$(r * s)_n = \sum_m r_m s_{n-m}. \quad (1)$$

If the Fourier transform of  $r_m$  is concentrated within a certain frequency band, the convolution  $(r * s)_n$  rejects

Fourier components of the signal outside this band. One can generate a succession of band-limited functions by discretizing and rescaling a suitable continuous-time function called an 'analysing wavelet'. By convolving a data series with a succession of such functions, one decomposes the signal into time-varying contributions from different (but possibly overlapping) frequency bands. An analysing wavelet  $g(t)$  has discrete representations (Kronland-Martinet, Morlet & Grossman 1987)

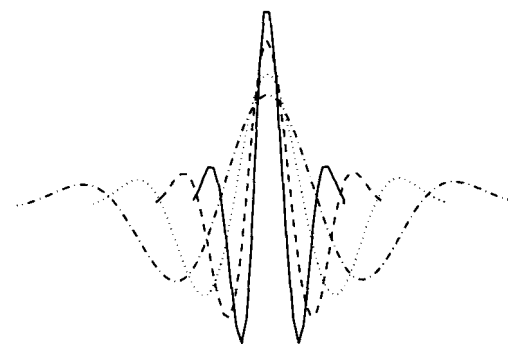
$$g_m^a = c_a g\left(\frac{t}{a}\right); \quad t = m \Delta t \quad (2)$$

where  $a$  is a scale parameter and  $c_a$  is a normalization factor that depends on  $a$ . By varying the scale parameter  $a$ , that is, by forming  $g_m$  that are stretched or compressed in time, one shifts the central frequency  $f_c$  and stretches the targeted frequency interval (Fig. 1). The wavelet transform of a discrete time series  $s_n$  is a convolution with the *time-reversed* wavelet,

$$\mathcal{T}[s](a, b) = (\hat{g}^a * s)_b = \sum_m \hat{g}_m^a s_{b-m}, \quad (3)$$

where  $g_m^a = \hat{g}_{-m}^a$ , we have assumed that the  $g_m^a$  are finite in

### Time Domain Wavelets



### Frequency Domain

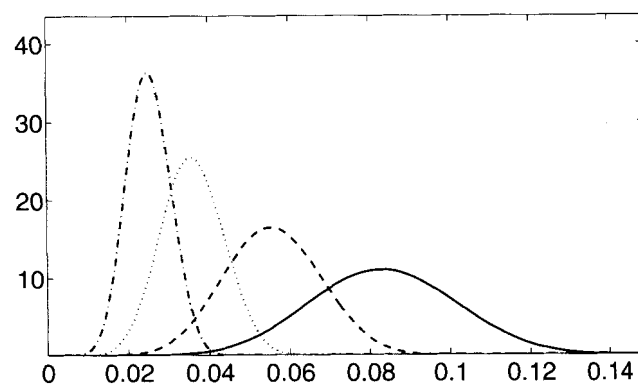


**Figure 1.** Scaling of a wavelet in the time and frequency domains. (Top) The discrete Slepian wavelets with time-bandwidth product  $p=2$  and time-bandcentre product  $p_c=2.5$ , optimized for resistance to spectral leakage. Slepian wavelets are asymptotically self-similar as their length increases. (Bottom) The discrete Fourier transforms of the Slepian wavelets. As wavelet length increases, sensitivity in the frequency domain shifts to lower frequencies.

time, and the scale parameter  $a$  and lag time  $b$  are allowed to vary continuously. The data series is set to zero outside the sampled interval. When the lag parameter  $b$  is less than a half-wavelet-length from the extremes of the time series, the wavelet transform is subject to 'edge effects', since the convolution (3) will extend outside the data interval.

We take a related, but different, approach to estimate the time-varying power spectrum  $\mathcal{P}(f, t)$ . The wavelets we use are not the discretized versions of a continuous-time function, but are the numerical solutions to an eigenvalue problem, constructed to maximize energy in a frequency band  $\{|f - f_c| \leq f_w\}$  about  $\pm f_c$ . We substitute explicit dependence on  $f_c$  for the scale parameter  $a$  used in eq. (2), writing

$$g_m(f_c), \quad m = -M/2 + 1, -M/2 + 2, \dots, M/2, \quad (4)$$

where dependence of the wavelet length  $M$  on the central frequency  $f_c$  is understood. The square of the wavelet transform at a point  $(f_c, t)$  provides an estimate of the signal's time-varying power spectrum  $\mathcal{P}(f_c, t)$ , averaged over the time window of length  $\Delta T = M \Delta t$  centred on  $t = n \Delta t$  and the frequency band  $\{|f - f_c| \leq f_w = \Delta f/2\}$ . We denote this estimated spectrum by  $\hat{\mathcal{P}}(f_c, t)$ .

The area in the time-frequency plane over which spectral information is averaged can be expressed as  $2p = \Delta f \Delta T$ , where  $p = f_w \Delta T$  is the dimensionless time-bandwidth product. Both the moving-window DFT and the wavelet spectrum estimator average over fixed areas in the time-frequency plane. The trade-off between time and frequency resolution in a moving-window DFT is fixed by the choice of window length. In a wavelet transform the time resolution and the frequency resolution are not themselves fixed, but vary inversely in relation to each other. The time-scale over which changes can be resolved remains proportional to the period of interest; the frequency resolution changes accordingly, improving towards zero frequency. This difference from the moving-window DFT may be advantageous in the analysis of seismic signals, which can contain both band-concentrated oscillations and sudden, closely spaced arrivals.

In designing wavelets for spectrum estimation, there are two properties to optimize: (1) the wavelet should be localized in frequency without sacrificing localization in time; and (2) our spectrum estimate should have low variance without suffering from excessive bias. These two properties are closely related (Slepian 1983; Thomson 1982, 1990; Park, Lindberg & Vernon 1987a). The 'ideal' wavelet for our spectrum estimation problem has uniform energy inside  $\Delta f \Delta T$  and zero energy outside. This requires a function that has finite support both in time and frequency, a condition which is not realizable (Slepian 1983). However, the solutions to the appropriate eigenvalue problem are time-limited and nearly band-limited functions, similar to the discrete prolate spheroidal sequences of Slepian (1978) and Thomson (1982). Using a family of finite-time wavelets that are optimally concentrated in the frequency domain, we can derive a number of statistically independent spectrum estimates that possess excellent resistance to spectral leakage. These can be combined into a single, low-variance spectrum estimate.

Consider a function of discrete time  $\{w_m\}_{m=-M/2+1}^{M/2}$  with a unit sample spacing  $\Delta t = 1$ . The kernel of this section in the

frequency domain is given by its discrete Fourier transform (DFT)

$$W(f) = \sum_{m=-M/2+1}^{M/2} w_m e^{i2\pi f m}, \quad (5)$$

where  $f$  is a continuous variable in the interval  $|f| \leq 1/2$ . The 'energy' of  $w_m$  is the magnitude squared of  $W(f)$ :

$$\mathcal{E}_w(f) = |W(f)|^2 \quad (6)$$

We seek a function  $w_m$  which has its spectral energy optimally concentrated within a band  $|f - f_c| \leq f_w$ . Real-valued wavelets will also concentrate energy in the mirror image of this band  $|f + f_c| \leq f_w$  at negative frequency. We parametrize the time-bandwidth product for Slepian wavelets using the positive frequency interval only. We wish to maximize the ratio of the wavelet's spectral energy within the targeted band to its total energy integrated over all frequencies. We designate this ratio as  $\lambda$ :

$$\lambda(M, f_c, f_w) = \frac{\int_{f_c - f_w}^{f_c + f_w} |W(f)|^2 df + \int_{-f_c - f_w}^{-f_c + f_w} |W(f)|^2 df}{\int_{-1/2}^{1/2} |W(f)|^2 df}. \quad (7)$$

The numerator can be written instead as a difference of two integrals, each with limits that are symmetric about zero frequency:

$$\lambda(M, f_c, f_w) = \frac{\int_{-(f_c + f_w)}^{f_c + f_w} |W(f)|^2 df - \int_{-(f_c - f_w)}^{f_c - f_w} |W(f)|^2 df}{\int_{-1/2}^{1/2} |W(f)|^2 df}. \quad (8)$$

Since only a signal of infinite duration can be completely band-limited,  $\lambda < 1$  for finite  $M$  and non-trivial  $f_w$  (Slepian 1983). We seek functions  $\{w_m\}$  whose  $W(f)$  maximize  $\lambda$ .

Following Thomson (1982) and Park *et al.* (1987a), we substitute the definition of the DFT (5) into (8), converting the optimization condition into matrix form:

$$\lambda(M, f_c, f_w) = \frac{\mathbf{x} \mathbf{C}^{(+)} \mathbf{x} - \mathbf{x} \mathbf{C}^{(-)} \mathbf{x}}{\mathbf{x} \cdot \mathbf{x}} = \frac{\mathbf{x} (\mathbf{C}^{(+)} - \mathbf{C}^{(-)}) \mathbf{x}}{\mathbf{x} \cdot \mathbf{x}}, \quad (9)$$

where the matrices  $\mathbf{C}^{(+)}$  and  $\mathbf{C}^{(-)}$  have components

$$\mathbf{C}_{tt'}^{(+)} = \frac{\sin [2\pi(f + f_w)(t - t')]}{\pi(t - t')}, \quad (10)$$

$$\mathbf{C}_{tt'}^{(-)} = \frac{\sin [2\pi(f - f_w)(t - t')]}{\pi(t - t')}. \quad (11)$$

This leads to the matrix eigenvalue problem

$$(\mathbf{C}^{(+)} - \mathbf{C}^{(-)}) \mathbf{x} - \lambda(M, f_c, f_w) \mathbf{x} = 0, \quad (12)$$

which may be compared with eq. 5 of Park *et al.* (1987a). The solutions to this problem are the ordered eigenvalues  $1 > \lambda_0 > \lambda_1 > \dots > \lambda_{M-1} > 0$  and the associated eigenvectors  $\psi_m^{(0)}, \psi_m^{(1)}, \dots, \psi_m^{(M-1)}$ , defined for  $m = -M/2 + 1,$

**Table 1.** Eigenvalues of eq. (14) for  $1/f_c = 19.874$  s. The above numbers can be interpreted as the percentage of the corresponding eigenwavelet energy that is concentrated within the frequency band  $\{|f - f_c| \leq f_w\}$ , where  $f_w = p/(M \Delta t)$  and  $f_c = p_c/(M \Delta t)$ .

k	$p=2.5, p_c=3.0$	$p=3.5, p_c=7.0$
0	0.99999983673037	0.9999999757913
1	0.9999927773380	0.9999999612377
2	0.99996444801934	0.9999980427057
3	0.99995472359615	0.9999955700883
4	0.99917777927764	0.99999211041072
5	0.99632632385259	0.99997984082360
6	0.98529850559400	0.99979052709721
7	0.94375942806624	0.99951515844152
8	0.79209507091359	0.99611715642462
9	0.70107195680768	0.99298604452960
10	0.29478900153143	0.95364961906103
11	0.21648138308430	0.93762670085702
12	0.05999721307099	0.71831953094124
13	0.01002665667556	0.69901079611901
14	0.00095739924610	0.29851357100145
15	0.00009441675733	0.28148896868200
16	0.00000611412342	0.06369473165561
17	0.00000044245031	0.04640458518342
18	0.00000002123842	0.00796436283757
19	0.00000000118487	0.00397119220161

$-M/2 + 2, \dots, M/2$ . The  $\lambda_i$  represent the fraction of spectral energy concentrated within the chosen frequency band. As a result,  $\psi_m^{(0)}$  is the function of length  $M$  which comes nearest to being band-limited within  $\Delta f$ . Approximately the first  $4Mf_w \Delta t = 2 \Delta f \Delta t$  eigenvectors are usefully concentrated in frequency. The factor of 2 arises from using both positive and negative frequency intervals in the optimization condition (7).

The  $\psi^{(i)}$  eigenvectors are functions of  $M, f_w$ , and  $f_c$ , but can be more conveniently expressed in terms of  $f_c$  and two dimensionless variables, the time-bandwidth product  $p = f_w \Delta T = f_w M \Delta t$  and a similar 'time-bandcentre' product  $p_c = f_c \Delta T = f_c M \Delta t$ :

$$\psi^{(i)} = \psi^{(i)}(f_c, p, p_c). \tag{13}$$

We refer to these functions as 'Slepian wavelets', or as 'eigenwavelets', in keeping with the terminology of multitaper techniques. Condition (8) yields, for given values of  $p$  and  $p_c$ , a family of approximately  $4p$  orthogonal wavelets for each frequency band that have desirable spectral leakage properties. We normalize the eigenwavelets so that

$$\sum_{m=-M/2+1}^{m=M/2} (\psi_m^{(k)})^2 = 1. \tag{14}$$

Wavelets with a fixed value of time-bandwidth product  $p$  are referred to as  $p\pi$  Slepian wavelets (Figs 2 and 3). When

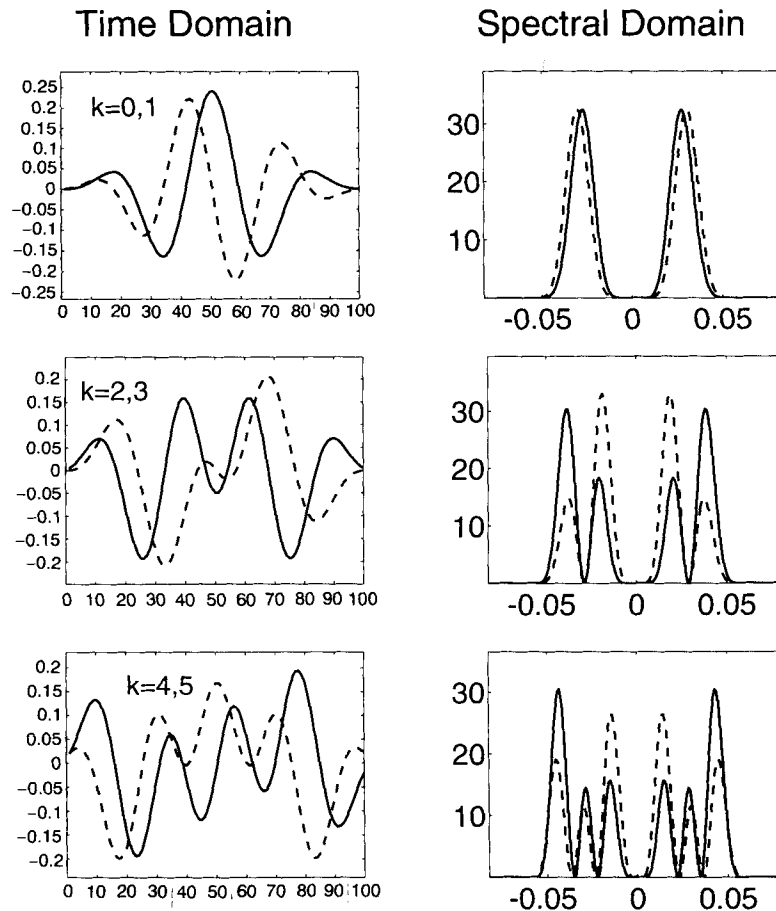


**Figure 2.** The first six Slepian wavelets with time-bandwidth product  $p = 2.5$  and time-bandcentre product  $p_c = 3.0$ . The discrete wavelets are grouped in pairs of odd and even functions with similar spectral sampling properties. This choice of  $p, p_c$  corresponds to a time-concentrated Slepian wavelet family.

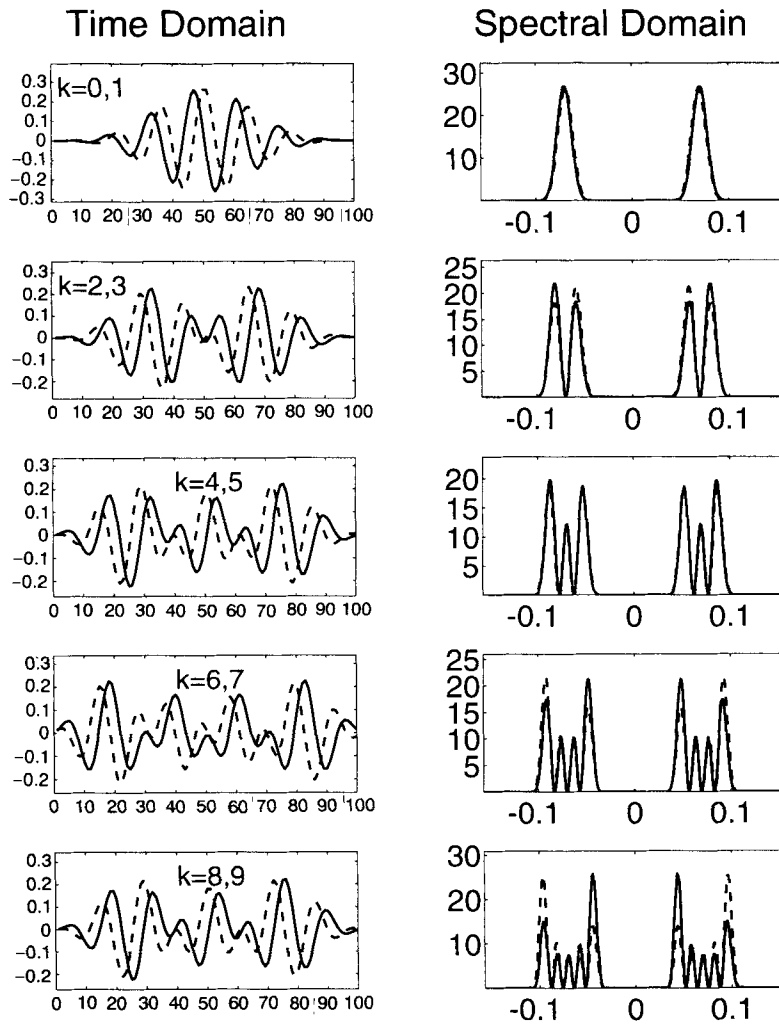


**Figure 3.** The first 10 Slepian wavelets, optimized for spectral leakage, with time-bandwidth product  $p = 3.5$  and time-bandcentre product  $p_c = 7.0$ . The discrete wavelets are grouped in pairs of odd and even functions with similar spectral sampling properties. This choice of  $p$ ,  $p_c$  corresponds to a frequency-concentrated Slepian wavelet family.

information from different Slepian wavelets is combined, one obtains a more even weighting of spectral information in the specified  $\Delta f \Delta T$  rectangle in the time-frequency plane (Fig. 4).

Strictly speaking, the Slepian wavelets fail to satisfy one of the defining characteristics of a 'wavelet', as they are not interpolates of a single function of continuous time. However, if both  $p$  and  $p_c$  are held constant and  $M$  is sufficiently large, the resulting functions  $\psi_m^{(i)}(f_c)$  approximate scaled versions of each other. In practice, we have used numerical spline approximations for the longer Slepian wavelets ( $M > 200$ ), and these are self-similar.

Slepian wavelets resemble, but are not equal to, Slepian tapers multiplied by sines and cosines. Intuitively, one might expect a band-limited wavelet to be equivalent to a band-limited taper with central frequency translated from  $f = 0$  to  $f = f_c$ . In most wavelet applications, however, the ratio  $f_w/f_c$  is large enough that the sidelobes of the less leakage-resistant Slepian tapers overlap significantly in the frequency interval  $(-f_c + f_w, f_c - f_w)$ . This would lead to non-orthogonality among wavelets, which would degrade their statistical advantages. To avoid this, the optimization

condition (7) incorporates both positive and negative frequency intervals explicitly. One undesirable consequence of this formulation is that the Slepian wavelets cannot be calculated as the eigenvectors of a tridiagonal matrix (Slepian 1978), as can the Slepian tapers—see Grunbaum (1981a, b).

The 'multiwavelet transform' of a data series  $\{s_n\}$  has  $K$  values  $\mathcal{T}_k[s](f_c, n \Delta t)$  for every point  $(f_c, t) = (f_c, n \Delta t)$ , one for each Slepian wavelet used. These  $K$  values can be collected in a column vector  $\mathbf{m}[s](f_c, n \Delta t)$ , where

$$\mathbf{m}[s](f_c, n \Delta t) = \begin{bmatrix} \mathcal{T}_0[s](f_c, n \Delta t) \\ \mathcal{T}_1[s](f_c, n \Delta t) \\ \vdots \\ \mathcal{T}_{K-1}[s](f_c, n \Delta t) \end{bmatrix}. \quad (15)$$

We define a simple wavelet estimator  $\hat{\mathcal{P}}(f_c, n \Delta t)$  of the power spectrum  $\mathcal{P}(f_c, n \Delta t)$  as an average of the  $K$  'eigenspectra':

$$\hat{\mathcal{P}}(f_c, t) = \frac{2}{K} \mathbf{m}^T[s](f_c, t) \cdot \mathbf{m}[s](f_c, t), \quad (16)$$

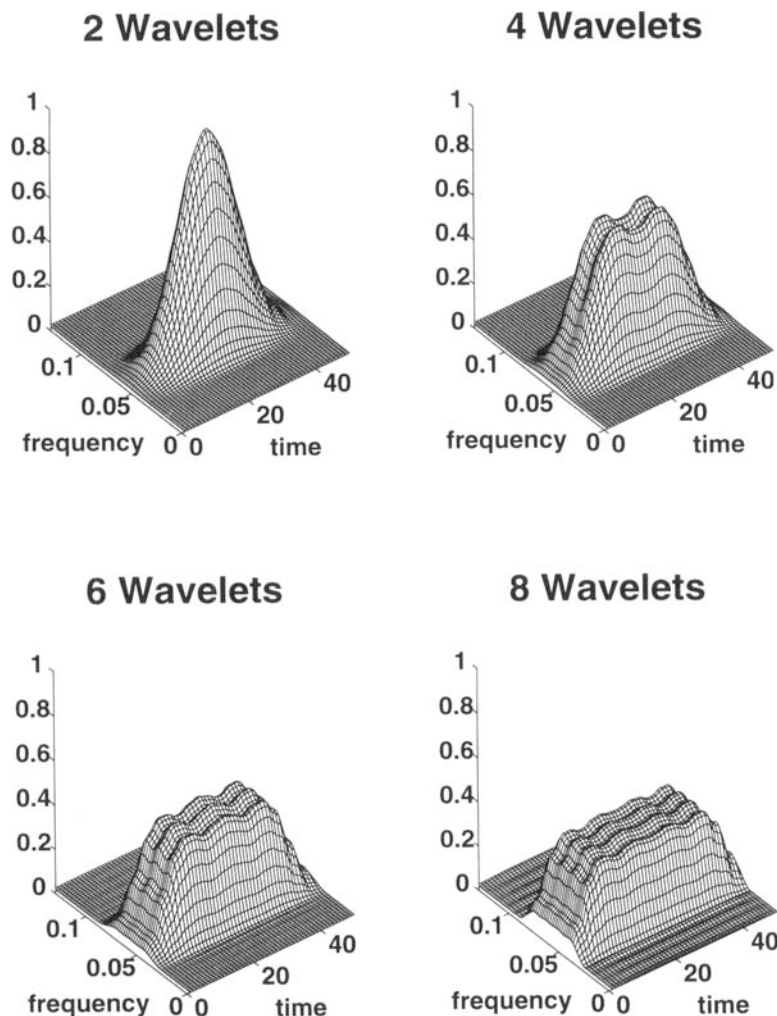


**Figure 4.** Coverage of the time–frequency window  $\Delta f \Delta T$  by weighted sums of Slepian wavelets with length  $M = 100$ , time–bandwidth product  $p = 3$  and time–bandcentre product  $p_c = 6$ . The wavelets are mutually orthogonal. Their squared discrete Fourier transforms are optimally concentrated in the interval  $0.015 < f < 0.045$ , where  $f_N = 0.5$  is the Nyquist frequency. The time-domain sensitivity is expressed as  $\sum_{k=0}^{K'} \sum_{m=1}^M (\psi_m^{(k)})^2$  for  $K' = 1, 2, 5$  and  $7$ . The frequency-domain sensitivity is expressed as  $\sum_{k=0}^{K'} |\Psi^{(k)}(f)|^2$  for  $K' = 1, 3, 5$  and  $7$ , where  $\Psi^{(k)}(f)$  is the DFT of the  $k$ th wavelet.

where the superscript ‘T’ denotes the transpose operator. The factor of 2 is introduced by grouping the Slepian wavelets into pairs of even and odd discrete functions, by analogy with the sines and cosines within the complex exponential  $\exp(-i2\pi f_c t)$ . In so doing, we anticipate the introduction of complex-valued Slepian wavelets in the next section. Since eq. (16) averages  $K$  estimates drawn from statistically independent samplings of the data,  $\hat{\mathcal{P}}(f_c, t)$  will have low variance without compromising a narrow time–frequency window  $\Delta f \Delta T$ . More sophisticated spectrum estimators can be computed from the  $\mathcal{T}_k$ , using the bandwidth retention factors  $\lambda_k$  as weights. In particular, a ‘high-resolution’ spectrum estimator, useful for white processes, weights the  $k$ th Slepian wavelet transform by  $\lambda_k^{-1}$ . An adaptive spectrum estimator, useful for coloured processes, can be constructed by downweighting—where the spectrum has relatively low amplitude—the spectrum estimates from less leakage-resistant wavelets. Its calculation is similar to that of the adaptive multitaper spectrum

estimator for stationary time series—see Thomson (1982), Park *et al.* (1987a) and Percival & Walden (1993) for details.

#### MULTI-WAVELET POLARIZATION ANALYSIS

The wavelet transform can estimate the time-varying cross-correlation of three-component seismic data, using the different  $\mathcal{T}_1[s](f_c, n \Delta t)$ ’s as independent ‘data’ retrieved from a chosen frequency interval. The singular value decomposition (SVD) estimates the ‘principal polarization’ of seismic particle motion. The singular values and singular vectors of the SVD can be used to reconstruct the time-domain signal associated with the principal polarization. The notation used below is taken from Park, Vernon & Lindberg (1987b), in which Slepian tapers were used to estimate the polarization of seismic motion (see also Vidale 1986; Jurkevics 1988; Wagner & Owens 1993, 1995).

At each point  $(f_c, t)$  of the wavelet transform, form the multiwavelet transform matrix  $\mathbf{M}$ , where

$$\mathbf{M}(f_c, t) = \begin{bmatrix} \mathcal{T}[x^1]_0(f_c, t) & \mathcal{T}[x^2]_0(f_c, t) & \mathcal{T}[x^3]_0(f_c, t) \\ \mathcal{T}[x^1]_1(f_c, t) & \mathcal{T}[x^2]_1(f_c, t) & \mathcal{T}[x^3]_1(f_c, t) \\ \vdots & \vdots & \vdots \\ \mathcal{T}[x^1]_{K-1}(f_c, t) & \mathcal{T}[x^2]_{K-1}(f_c, t) & \mathcal{T}[x^3]_{K-1}(f_c, t) \end{bmatrix}, \quad (17)$$

where the  $j$ th column of  $\mathbf{M}$  contains the multiple wavelet transforms of the  $j$ th data series  $x_n^j$ . The SVD of  $\mathbf{M}(f_c, t)$  is

$$\mathbf{M} = \mathbf{U}\mathbf{D}\mathbf{V}^H, \quad (18)$$

where  $\mathbf{U}$  is a  $K \times K$  unitary matrix,  $\mathbf{V}$  is a  $3 \times 3$  unitary matrix, and  $\mathbf{D}$  is a  $K \times 3$  diagonal matrix. The superscript 'H' denotes Hermitian conjugate—this reduces to the ordinary matrix transpose when  $\mathbf{V}$  is real-valued. The first three diagonal elements of  $\mathbf{D}$ , denoted  $d_j$ ,  $j = 1, 2, 3$ , are the singular values of  $\mathbf{M}$  with  $d_1 \geq d_2 \geq d_3 \geq 0$ . The columns of  $\mathbf{U}$  and  $\mathbf{V}$  correspond to, respectively, eigenvectors  $\hat{\mathbf{u}}_j$  of  $\mathbf{M}\mathbf{M}^H$  and eigenvectors  $\hat{\mathbf{v}}_j$  of  $\mathbf{M}^H\mathbf{M}$ . We refer to the  $\hat{\mathbf{u}}_j$  and the  $\hat{\mathbf{v}}_j$  as the left- and right-singular vectors of  $\mathbf{M}$ , respectively. By analogy to Park *et al.* (1987a), the wavelet estimator of the time-varying spectral density matrix  $\mathbf{S}(f, t)$  is  $\hat{\mathbf{S}}(f_c, t) = 2\mathbf{M}^H\mathbf{M}/K$ , where  $K$  is the number of real-valued wavelets used.

The first three left-singular vectors form an orthonormal basis set for the column space of  $\mathbf{M}$ . If we rotate  $\mathbf{M}$  by  $\mathbf{V}$ ,

$$\mathbf{M}\mathbf{V} = \mathbf{U}\mathbf{D} = [d_1\hat{\mathbf{u}}_1 \quad d_2\hat{\mathbf{u}}_2 \quad d_3\hat{\mathbf{u}}_3], \quad (19)$$

we obtain the left-singular vectors weighted by their corresponding singular values. The columns of this matrix represent spectrum estimates along each of three axes. If  $d_1 \gg d_2, d_3$ , nearly all of the spectral energy of  $\mathbf{M}$  is explained by motion along a single element of the rotated basis set. The components of  $\hat{\mathbf{v}}_1$  are direction cosines of this motion relative to the seismometer components, so that  $\hat{\mathbf{v}}_1$  corresponds to the principal polarization vector.

Since the  $K$  Slepian wavelets  $\psi^{(k)}(f_c)$  form an approximate basis for functions band-limited to  $(f_c - f_w, f_c + f_w)$ , a linear combination of the wavelets approximates the band-limited signal associated with the principal polarization in the neighbourhood of  $(f_c, t)$ . The coefficients of this linear combination are the components of the first left-singular vector  $\hat{\mathbf{u}}_1$  of  $\mathbf{M}$ . We denote this reconstructed signal as

$\hat{\mathbf{x}}(f_c, t)$ , where

$$\hat{\mathbf{x}}(f_c, t) = \begin{bmatrix} \psi_{-M/2+1}^{(0)} & \psi_{-M/2+1}^{(1)} & \psi_{-M/2+1}^{(2)} & \cdots & \psi_{-M/2+1}^{(K-1)} \\ \psi_{-M/2+2}^{(0)} & \psi_{-M/2+2}^{(1)} & \psi_{-M/2+2}^{(2)} & \cdots & \psi_{-M/2+2}^{(K-1)} \\ \vdots & \vdots & \vdots & \vdots & \vdots \\ \psi_{M/2}^{(0)} & \psi_{M/2}^{(1)} & \psi_{M/2}^{(2)} & \cdots & \psi_{M/2}^{(K-1)} \end{bmatrix} \times d_1\hat{\mathbf{u}}_1. \quad (20)$$

The largest singular value  $d_1$  identifies the polarization that explains the largest fraction of the total seismic energy at  $(f_c, t)$ . To determine whether the principal polarization is significant in a statistical sense, we compare its energy to the total in all three polarizations. Following Mann & Park (1994), we use a test on the normalized first singular value  $\bar{d}_1$ , where

$$\bar{d}_1 = \frac{d_1}{\sqrt{d_1^2 + d_2^2 + d_3^2}}. \quad (21)$$

Significant coherent seismic energy is indicated when  $\bar{d}_1$  is close to unity, assuming that only one coherent signal exists in the neighbourhood of  $(f_c, t)$ . Robust determination of multiple signals will probably require multiple stations, for example a seismic array.

We obtain confidence levels for  $\bar{d}_1$  based on Monte Carlo simulations of the SVD, assuming that the seismic noise in each component is independent and can be approximated by Gaussian white noise. Since there is often much signal-generated noise in a seismic record, this is a highly simplified model. However, it is none the less useful as a null hypothesis. The orthonormality of the eigenwavelets implies that the multiple Slepian wavelet transform of an uncorrelated Gaussian data will also be uncorrelated Gaussian data, and that the  $k = 0 \cdots (K-1)$  spectrum estimates will be formally uncorrelated. It therefore suffices to fill the columns of  $\mathbf{M}$  with Gaussian white noise. We calculated the SVD of 10 000  $K \times 3$  matrices of Gaussian-distributed random numbers with uniform variance  $\sigma^2$ . The empirical probability density functions for  $\bar{d}_1$  for six  $2\pi$  and 10  $3\pi$  wavelets yielded the confidence levels given in Table 2.

Because the above development is based on real-valued wavelets, the principal polarization  $\hat{\mathbf{v}}_1$  is real-valued, and can represent only rectilinear motion. In order to detect coherent motion with elliptical polarization, the Slepian wavelets must be modified to be sensitive to phase shifts among the particle-motion components. In standard Fourier

**Table 2.** Confidence estimates for the normalized first singular value  $\bar{d}_1$ , based on the assumption that seismic noise in each component direction is Gaussian white noise. 10 000 Monte Carlo trials were performed.

% Confidence	2.5 $\pi$ real	3.5 $\pi$ real	2.5 $\pi$ complex	3.5 $\pi$ complex
99.99	0.972	0.932	0.989	0.952
99.9	0.954	0.916	0.979	0.932
99.	0.924	0.879	0.959	0.908
95	0.895	0.840	0.938	0.879
90	0.875	0.820	0.922	0.862
80	0.847	0.794	0.900	0.840

techniques, a linear combination of sines and cosines is represented as the real part of  $\exp[-i(2\pi ft + \phi)]$ , where  $\phi$  is the phase shift in radians. Because the Slepian wavelets appear in pairs of even and odd functions with similar frequency localization properties, we construct analogous complex-valued wavelets, e.g.  $\tilde{\psi}^{(0)} = (\psi^{(0)} + i\psi^{(1)})/\sqrt{2}$ .

Some care must be taken, however, to preserve the proper phase relationship between real and imaginary parts of the wavelet, which we prescribe to match a complex sinusoid  $\exp(-i2\pi ft)$ . A phase shift of  $\phi$  rad can be represented by taking the real part of  $e^{-i\phi}\tilde{\psi}^{(k)}$ .

A multiple wavelet transform  $\tilde{\mathcal{T}}_k[s](f_c, t)$  using  $\tilde{K}$

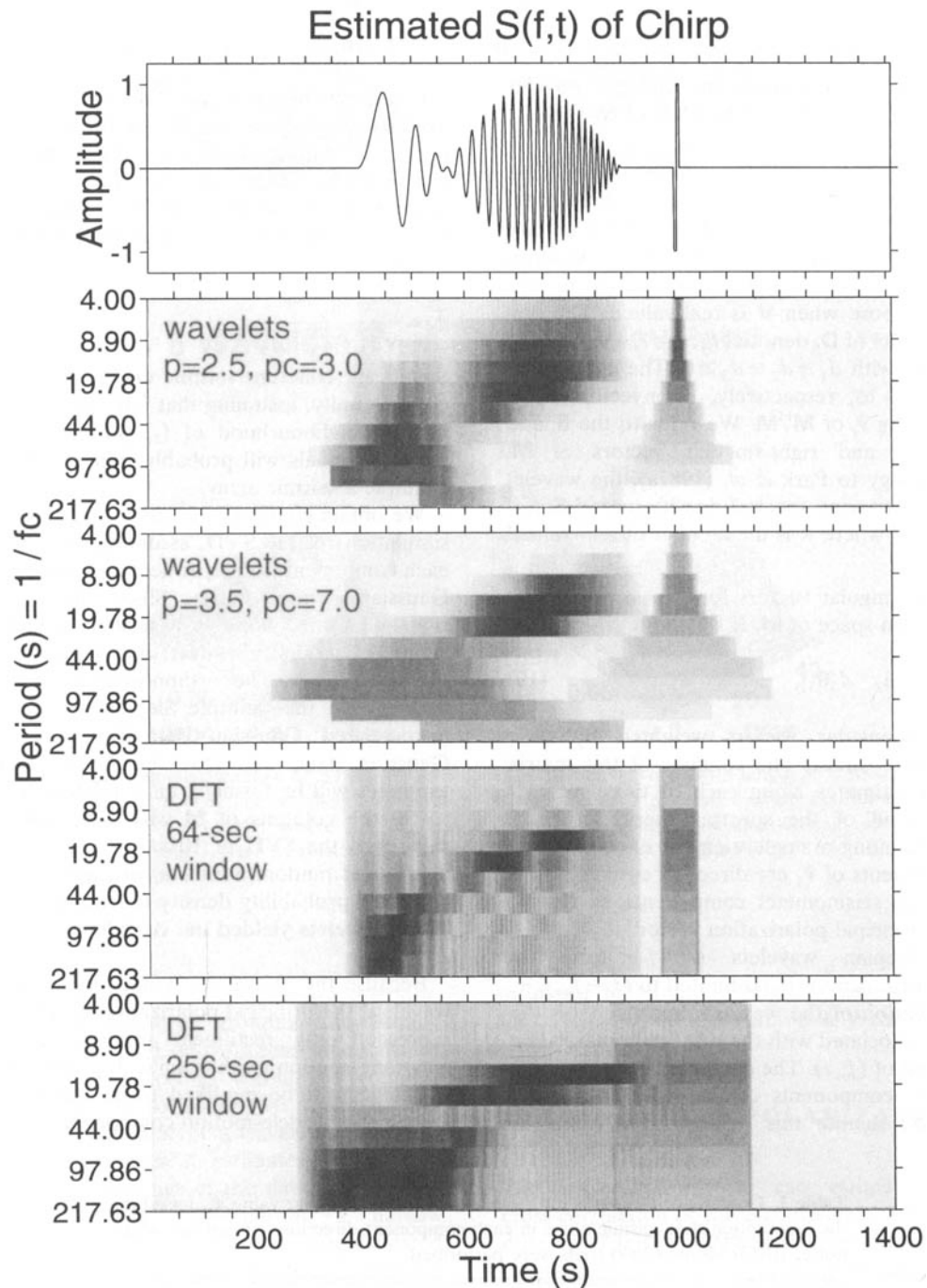


**Figure 5.** Multiwavelet spectral analysis of a notched chirp (shown in the top figure) with a 10 s square wave pulse following. Spectral estimates using the  $2.5\pi$  ( $p_c = 3.0$ ) and the  $3.5\pi$  ( $p_c = 7.0$ ) wavelets are compared with evolutive Fourier spectra using short (64 s) and long (256 s) time windows. The darkest shading corresponds to the highest spectrum values within that window. The values of the wavelet spectra are normalized by dividing by the square root of the length of the wavelet. The DFTs are linearly interpolated to frequencies corresponding to the central frequencies of the wavelet frequency bands, to allow a more direct comparison of time/frequency resolution. Notice the arrowhead features in the wavelet transforms, which point to sudden events, i.e. the square wave and the beginning of the chirp. The time-concentrated wavelets show the amplitude notch clearly. Spectra based on the long-window DFT, on the other hand, highlight the notch in the frequency domain, providing tighter frequency resolution in return for looser time resolution.

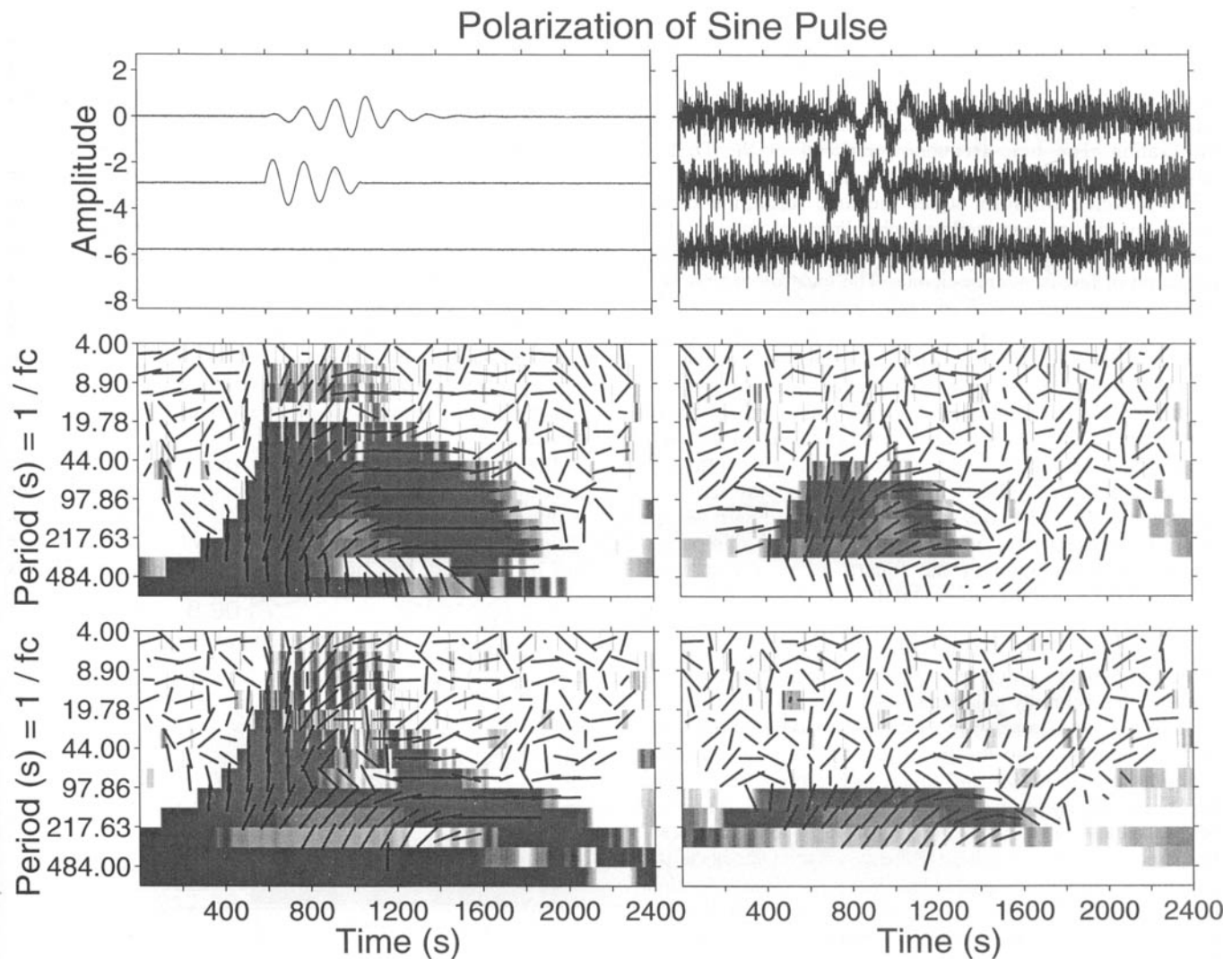


**Figure 6.** Multiwavelet polarization analysis of a synthetic sine pulse with two different signal-to-noise ratios. The polarization of the sine pulse changes from transverse to radial as its amplitude decreases. Left column: Gaussian white noise with variance  $\sigma^2 = 1/100$  has been added. Right column: Gaussian white noise with variance  $\sigma^2 = 1/2$  has been added. The correlation and polarization of both the low-noise data set (left column) and the high-noise data set (right column) are estimated using  $2.5\pi$  ( $p_c = 3.0$ ) and  $3.5\pi$  ( $p_c = 7.0$ ) wavelets (middle and bottom rows, respectively). The shading represents confidence estimates for correlated motion based on the Monte Carlo simulations, with white indicating less than 90 per cent and darkest gray  $\geq 99.99$  per cent confidence. Black bars represent the polarization in the horizontal plane at the points  $(f, t)$  corresponding to their mid-points. Right-left and up-down orientations in the plots signify radial and transverse motions, respectively. The length of each bar is proportional to the projection of the unit-normalized particle-motion ‘ellipse’ onto the horizontal plane. Note the frequency localization of the coherence estimator in the presence of significant noise, which erases spectral leakage effects.

complex-valued Slepian wavelets is computationally equivalent to a wavelet transform that uses the corresponding  $K = 2\bar{K}$  real-valued Slepian wavelets. The wavelet transforms using even wavelets correspond to the real part of  $\tilde{\mathcal{T}}_k[s]$ , while those using odd wavelets correspond to the imaginary part of  $\tilde{\mathcal{T}}_k[s]$ . The polarization analysis differs significantly, however, as the matrix  $\mathbf{M}$  has  $\bar{K}$  complex-valued rows in place of  $2\bar{K}$  real-valued rows. The SVD  $\mathbf{M} = \mathbf{U}\mathbf{D}\mathbf{V}^H$  likewise leads to complex singular vectors  $\hat{\mathbf{u}}_j$  and  $\hat{\mathbf{v}}_j$ . The right-singular vector  $\hat{\mathbf{v}}_1$  associated with the largest singular value is identified as the principal polarization, and the relative phases of its complex components determine the ellipticity of the polarization (Park *et al.* 1987b). The conditions for the statistical significance of the principal

polarization differ from those of the real-valued, purely rectilinear formulation, because the ‘signal’ associated with it has more degrees of freedom in its parametrization. We estimated confidence limits for non-randomness, relative to a white-noise assumption, with a 10 000 realization Monte Carlo simulation.

## SYNTHETIC EXAMPLES

We demonstrate the methods described in the preceding sections on several synthetic data sets. First, we compare the multiwavelet spectrum estimator (16) with a moving-window DFT. In Fig. 5 both techniques are applied to a time series

containing a notched 'chirp' function, a sinusoid with linearly increasing frequency and modulated amplitude, followed by one period of a high-frequency square wave. Each technique is applied twice, the first application adjusted for time-localization and the second for frequency-localization. The time-frequency trade-off of the DFT is adjusted by varying the length of the moving window.

The wavelet transform scales the time resolution to the frequency being examined, which allows a narrow time resolution at high frequencies while still allowing the detection of low-frequency signals. The location in time of a sudden event with energy at high frequencies, such as the square wave pulse, can be tightly constrained by the wavelet transform. The arrow-like shapes pointing to the location of the square wave in time are characteristics of the wavelet-transform representation of a time-limited broadband event. At the low-frequency end of the chirp, where the local period varies rapidly, a similar shape is confined to long-period bands. These features of the wavelet-based spectra contrast with the uniform time resolution of the Fourier-based spectra, which result in (for example) a box-like representation of the square wave. The moving-window DFTs, on the other hand, have better frequency resolution at high frequencies.

To test the correlation estimator (21), we use a three-component synthetic (Fig. 6, top), containing a sinusoid that is briefly polarized along one axis but rotates to another axis. Correlation estimates using both the time-concentrated and the frequency-concentrated wavelets are performed for high and low signal-to-noise ratios (Fig. 6). Where the noise level is very low, even a small amount of spectral leakage can bias the coherence estimate at distant frequencies. However, where there is a significant noise the coherence estimator locates the sine pulse tightly in time and frequency. The estimator may be adjusted, through an appropriate choice of wavelets, to highlight either time or frequency localization. Polarization estimates follow the transition of the wave from one orientation to another. Outside the correlated region the polarization appears randomly oriented.

The wavelet transform is often used as a way to decompose and reconstruct signals as faithfully as possible with a reduced number of parameters. Here we approach the different problem of reconstructing a correlated signal in noise, whether background or signal-generated, where an imperfect reconstruction is unavoidable. What is our motivation for this? A simple bandpass filter does not distinguish the stochastic from the correlated components of the signal. When a statistically significant polarization of seismic motion is found to exist, a reconstructed signal  $\hat{\mathbf{x}}$  can be formed as in eq. (20). The reconstructed local signal  $\hat{\mathbf{x}}$  can be rotated back onto the coordinate axes by multiplying  $\hat{\mathbf{x}}$  by  $\hat{\mathbf{v}}_1^H$ ; the result represents the bandpassed, correlated portion of each data set component. A local reconstruction centred at time  $t_0$  will tend to be more reliable near  $t_0$  than near the ends of the wavelet interval, where the wavelets tend to decrease in amplitude. It is therefore useful to combine the time-domain reconstructions from many overlapping time intervals. To incorporate statistical confidence estimates, we take a weighted average of reconstructions from every time interval in the region of interest. Following a fuzzy logic criterion, we chose unit

weighting for  $\bar{d}_1(t) > 99.99$  per cent confidence, based on the Gaussian white noise trials, and weights that decrease linearly to zero at a cut-off confidence (90 per cent or higher). This scheme is ad hoc but produces satisfactory reconstructions of synthetics immersed in noise.

Signals that have energy across frequency bands can be reconstructed by adding together the weighted-average reconstructions from a number of adjacent frequency bands. A data set that has the chirp/square wave signal from Fig. 5 along the transverse component is shown in Fig. 7. Neither set of wavelets reconstructs the signal with sufficient amplitude throughout its length, due to the poorer sensitivity of the wavelet transform at the extremes of frequency bands. Both choices of  $p$  and  $p_c$  reconstruct the square wave pulse at nearly the proper amplitude, although the time-concentrated wavelets introduce fewer spurious oscillations.

The limitations of using purely real wavelets, as in the previous examples, is that seismic motion in which the components oscillate out of phase will appear uncorrelated. Elliptical motion, such as in Rayleigh waves, will therefore not be detected; this provides the motivation for complex

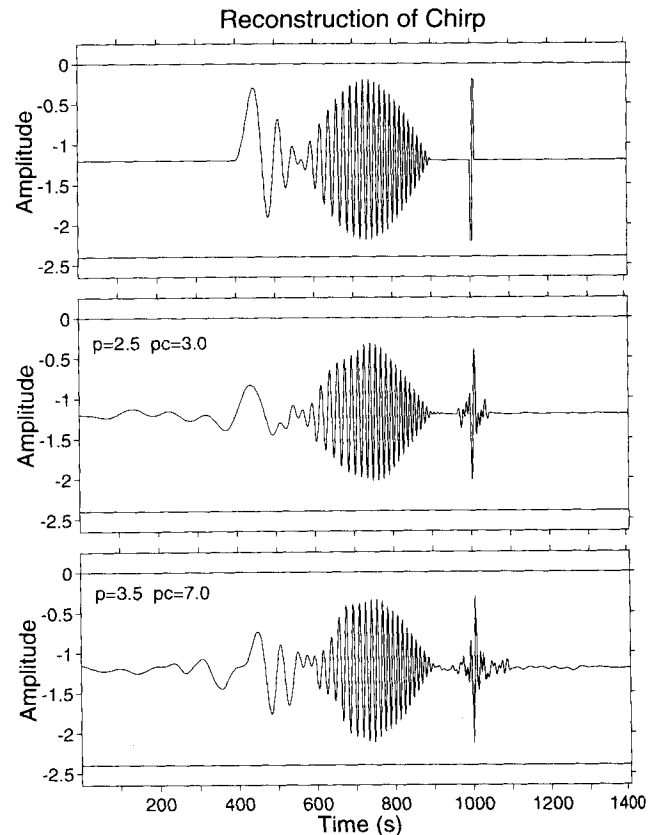


**Figure 7.** Broad-band multiwavelet reconstruction of a dispersive chirp and square wave, shown at the top. The transverse component is the time series from Fig. 5; the radial and vertical components above and below are zero. A reconstruction is a simple-minded sum of signals from adjacent frequency bands. The poorer response of the wavelets near the edges of their intervals of frequency concentration causes deficient amplitude in the high-frequency portion of the reconstructed chirp. The square wave and the early portion of the chirp, where frequency is changing rapidly, pose more of a difficulty for the longer wavelets (bottom).

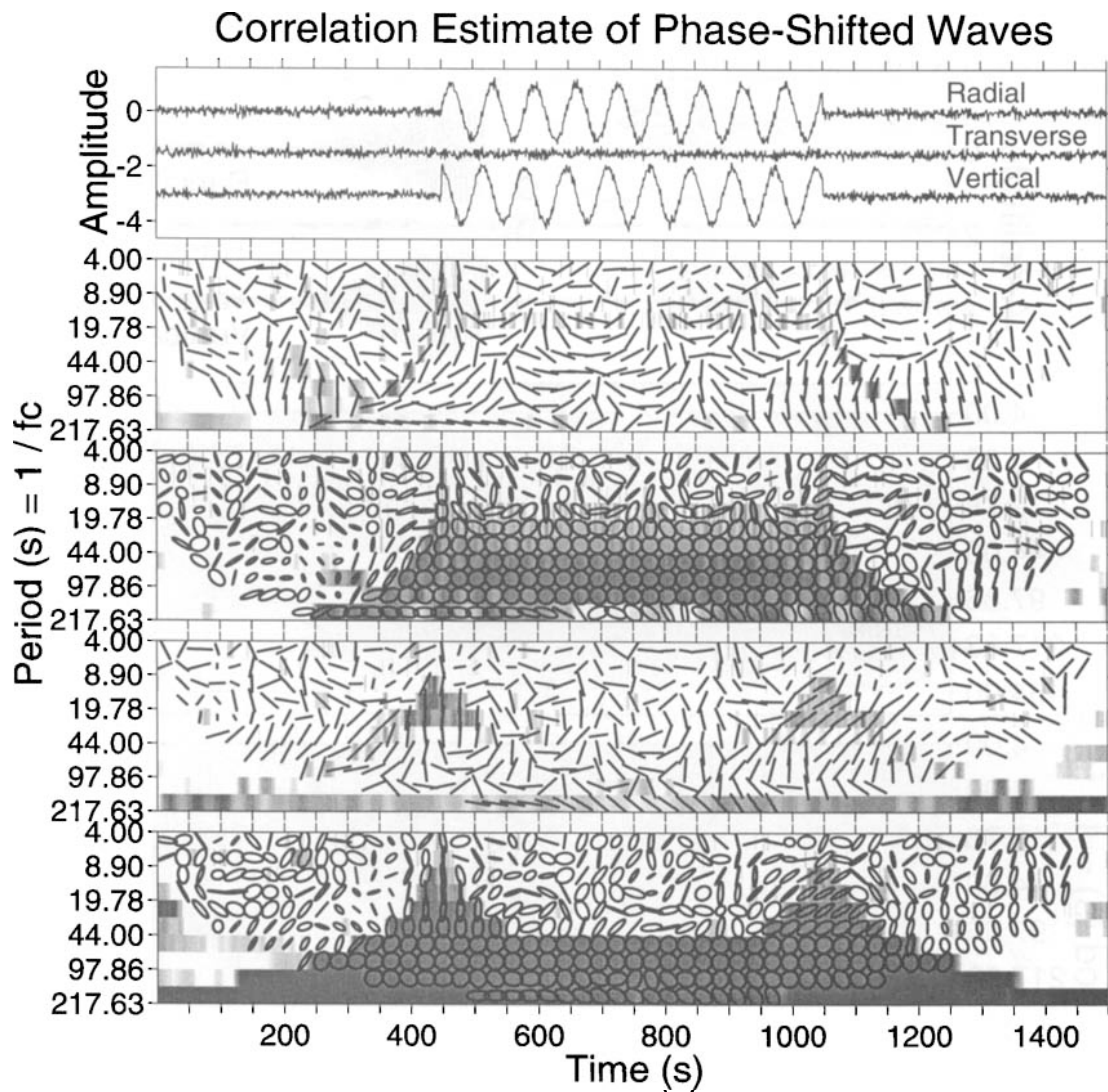


**Figure 8.** Multiwavelet analysis of a synthetic seismogram consisting of elliptically polarized radial and vertical components, with zero transverse motion. Gaussian white noise of uniform variance  $\sigma^2 = 1/10$  is added to obtain the data set shown at top. As in Fig. 6, shading indicates locations  $(f, t)$  where the confidence estimate for non-randomness of the normalized first singular value  $\bar{d}_1$  exceeds 90 per cent. The second and fourth plots (from the top) show polarization estimates in the radial-vertical plane using real  $2.5\pi$  and  $3.5\pi$  wavelets, respectively. Plotting conventions are identical to those in Fig. 6, except that up-down orientation represents vertical motion, instead of transverse. The elliptical signal is nearly invisible to the real-valued wavelets. The middle and bottom figures show polarization estimates using complex  $2.5\pi$  and  $3.5\pi$  wavelets, respectively. Ellipses in the radial-vertical plane are computed from the complex-valued principal polarization vector  $\hat{v}_1$ . Direction conventions are identical to the real-valued case, and indicate circular particle motion in the radial-vertical plane.

wavelets based on even-odd pairs (Fig. 8). The radial and vertical components of this synthetic seismic signal are two sinusoids, mutually out of phase by  $90^\circ$ . This elliptical motion is not detected by the real-valued wavelets.

#### APPLICATION TO SEISMIC DATA

The wavelet transform offers a fine-grained picture of seismic waveform behaviour in both time and frequency. We illustrate its uses with data from three recent earthquakes recorded by the Global Seismographic Network.

The 1991 February 9 event in the Solomon Islands, recorded at PAS (Pasadena, Calif.,  $\Delta = 89.3^\circ$ ) is an archetypal long-period seismogram. After propagation

across the Pacific Ocean basin, the surface waves appear simple (Fig. 9). This is borne out by the wavelet-based polarization analysis. The wavelet spectrum estimates for each particle-motion component are dominated by the fundamental Love and Rayleigh waves. The body waves preceding the surface waves appear as time-localized broad-band signals. Fig. 10 shows the values of the singular values  $d_1, d_2, d_3$  of the multiwavelet transform matrix  $\mathbf{M}$ —each plot is self-scaled to emphasize internal variations. The first singular value  $d_1$  is associated with the principal polarization as a function of time and frequency, and tends to maximize at the arrivals of the body and surface waves. Note the ‘C’ formed by the dispersed Rayleigh wave in the time-frequency plane, with correlated energy at the

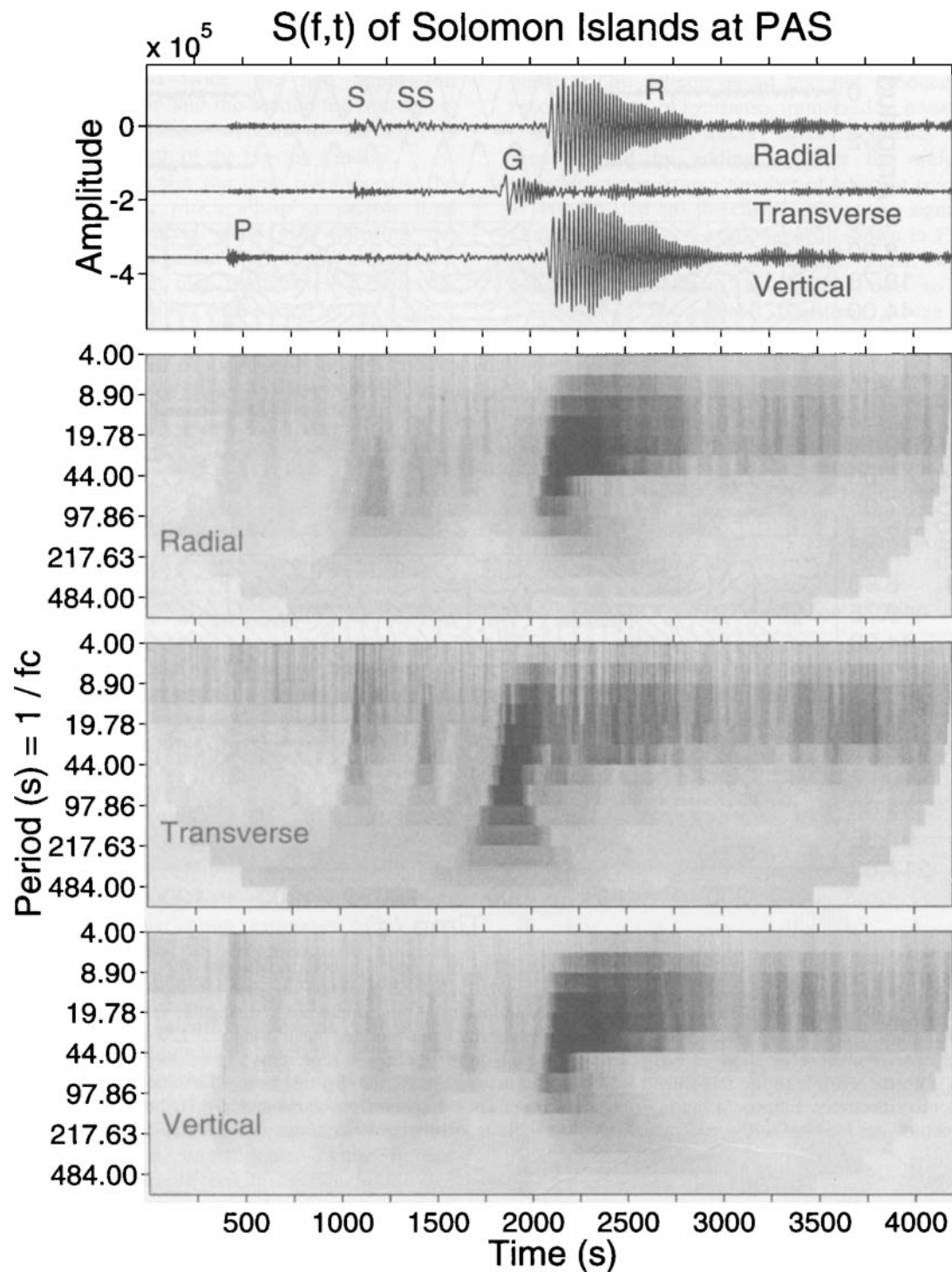


**Figure 9.** Multiwavelet spectral analysis of the 1991 February 9 Solomon Islands event (NEIC magnitude  $m_b = 6.9$ , location  $9.4^\circ\text{S}$ ,  $159.1^\circ\text{E}$ , depth 33 km), recorded at PAS (Pasadena, California,  $\Delta = 89.3^\circ$ ). The lower panels show the wavelet spectrum estimates for each component of motion. Our analysis uses three complex Slepian wavelets with  $p = 2.5$ ,  $p_c = 3.0$ . We set the spectrum estimates to zero wherever they are subject to bias from finite-record effects.

75–125 s group-velocity maximum followed by correlated energy at both shorter and longer periods. The second singular value  $d_2$  represents the largest parcel of energy except for the principal polarization. A large  $d_2$  could arise from multiple phase arrivals, multipathed surface waves or

scattering. The patterns of  $d_2$  and  $d_3$  are similar to that of  $d_1$  in this example, but less clearly organized. This suggests that much of the ‘noise’ in the seismogram is signal-generated.

Figure 11 shows the wavelet polarization estimates for rectilinear motion in the horizontal plane, and for elliptical

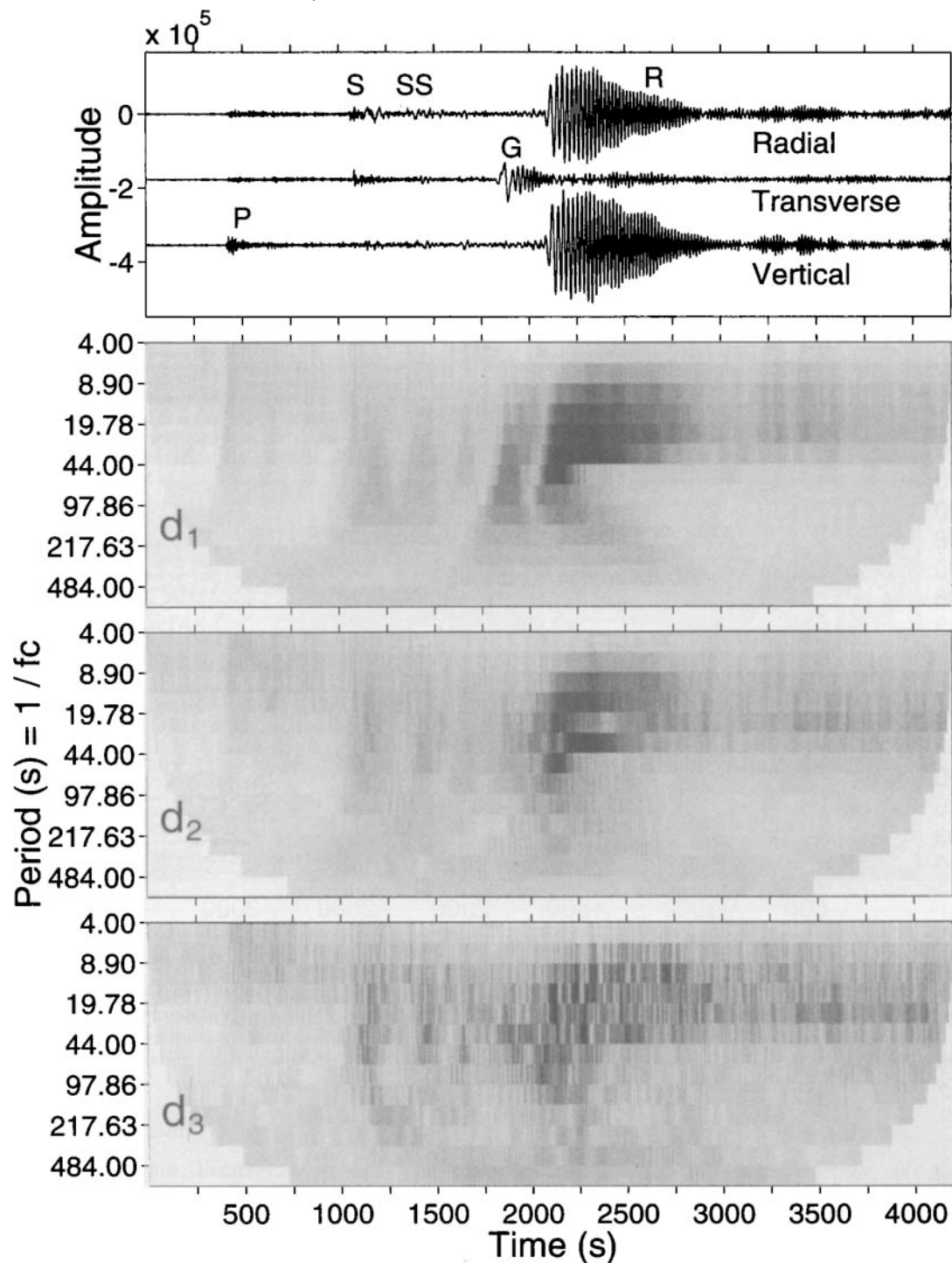


**Figure 10.** Multiwavelet SVD spectra of the 1991 February 9 Solomon Islands event recorded at PAS. Our analysis uses three complex Slepian wavelets with  $p = 2.5$ ,  $p_c = 3.0$ . The lower panels plot the singular values  $d_1$ ,  $d_2$ ,  $d_3$  of the multiwavelet transform matrix  $\mathbf{M}$ . The shading for each  $d_k$  is gain-ranged to emphasize relative maxima. The  $d_1$  spectrum shows the signal associated with the ‘principal polarization’. We set the singular values to zero wherever they are subject to bias from finite-record effects.

motion (using complex-valued wavelets) in both the horizontal and radial–vertical planes. The shading in the plot graphs values of  $\bar{d}_1$  at  $\geq 90$  per cent confidence. The polarization of particle motion is indicated on a coarser scale. The particle motion appears to be consistent within

patches where  $\bar{d}_1$  is significantly non-random, tending to fluctuate more where a single polarization does not dominate. The test for rectilinear polarization identifies the Love wave, but not the Rayleigh wave, as expected. The complex wavelets identify the dispersion of the fundamental

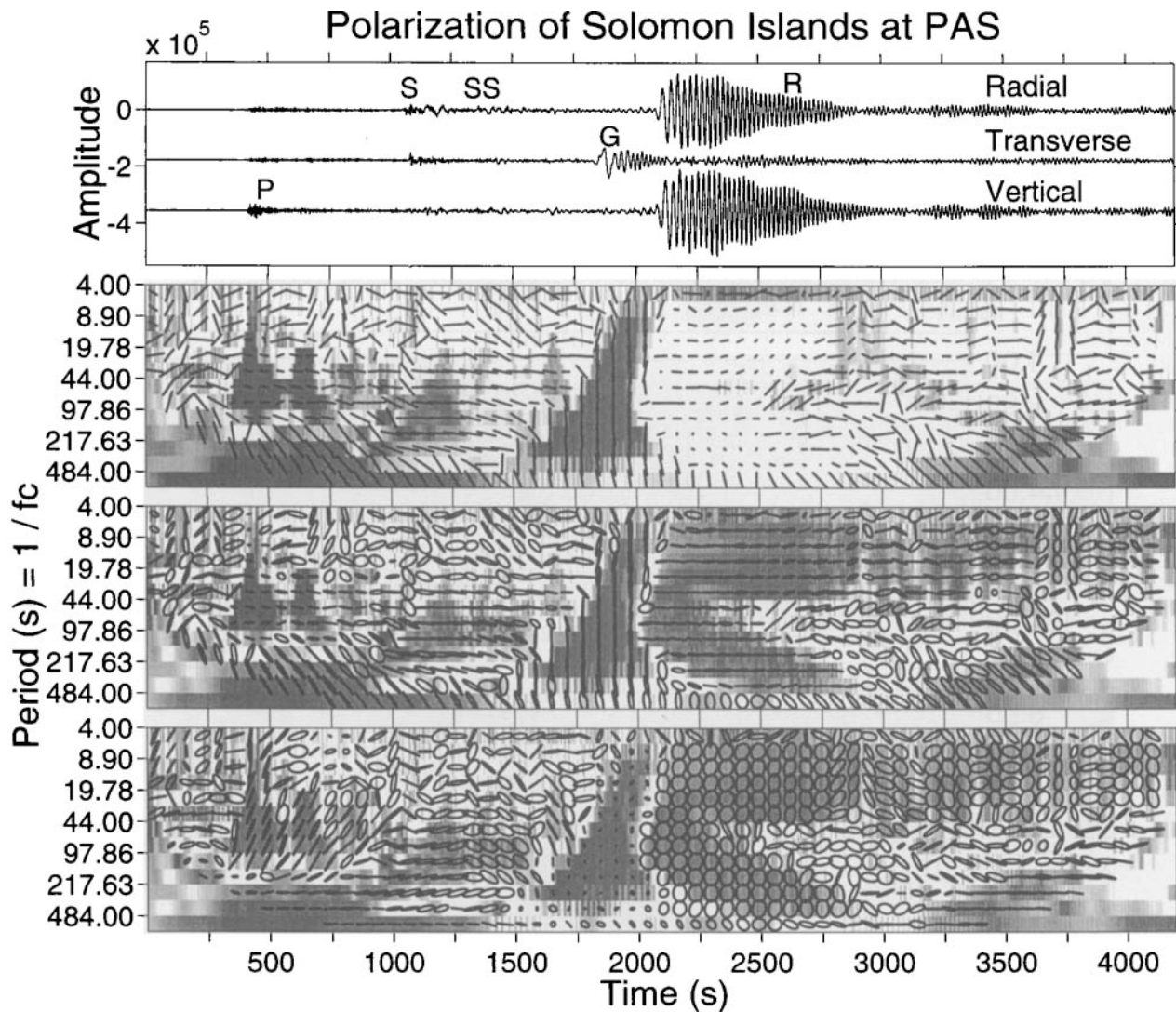


**Figure 11.** Multiwavelet polarization analysis of the 1991 February 9 Solomon Islands event recorded at PAS. Our analysis uses three complex Slepian wavelets with  $p = 2.5$ ,  $p_c = 3.0$ . In the lower panels the normalized first singular value  $\bar{d}_1$  of the multiwavelet transform matrix  $\mathbf{M}$  is shaded where it exceeds 90 per cent confidence for non-randomness. The centre panel shows particle motion in the horizontal plane, with the radial component oriented right–left, and the transverse component oriented up–down. The lower panel shows particle motion in the radial–vertical plane, with the radial component oriented right–left, and the vertical component oriented up–down.

Rayleigh wave, as well as elliptical motion in the neighbourhood of the long-period *SS* wave. Elliptical motion in the horizontal plane is often associated with low values of  $\bar{d}_1$ . Long-period ‘noise’ at PAS is coherently polarized, as evidenced by the persistent weak-amplitude correlated motion during the *P* and Rayleigh codas.

The 1994 June 9 event in Northern Bolivia (NEIC magnitude  $m_b = 7.8$ , location  $13.7^\circ\text{S}$ ,  $67.4^\circ\text{W}$ ) was remarkable for its depth (600 km) and size. Ekstrom (1994) reports a seismic moment  $M_0 = 3.0 \times 10^{28}$  dyn cm, twice the release of the 1970 deep Columbian event. The *P* waves for this event reveal great complexity, with several subevents over an interval of roughly 40 s, with evidence of rupture northwards along a horizontal plane (Beck *et al.* 1994; Okal *et al.* 1994). Multiwavelet spectra of particle motion at SJG (San Juan, Puerto Rico,  $\Delta = 31.6^\circ$ ) reveal an abrupt increase in transverse-component energy a few seconds after the

peak energy on the vertical component, suggesting intense scattering close to the receiver (Fig. 12). The sequence of apparent subevents within the *P* and *pP* waves is not identical, suggesting a complex rupture in both space and time. The *pP* phase traverses the upper mantle and crust three times, and so has little energy at short periods relative to the *P* phase, which traverses the Earth’s upper layers only once. The *P* phase, however, is deficient in spectral energy in the 3–5 s period range, relative to the *pP* phase. This leads the *P* wave to appear resonant, rather than impulsive. Several *P* phases from this event show broadly similar behaviour, with peak energy strongly concentrated in the time–frequency plane. A similar localization of *pP* energy in the SJG record, but at longer periods, suggests (1) a strongly frequency-dependent scattering or attenuation mechanism along the *P* ray path where it diverges from the *pP* path, or (2) a Doppler effect associated with a propagating rupture front.

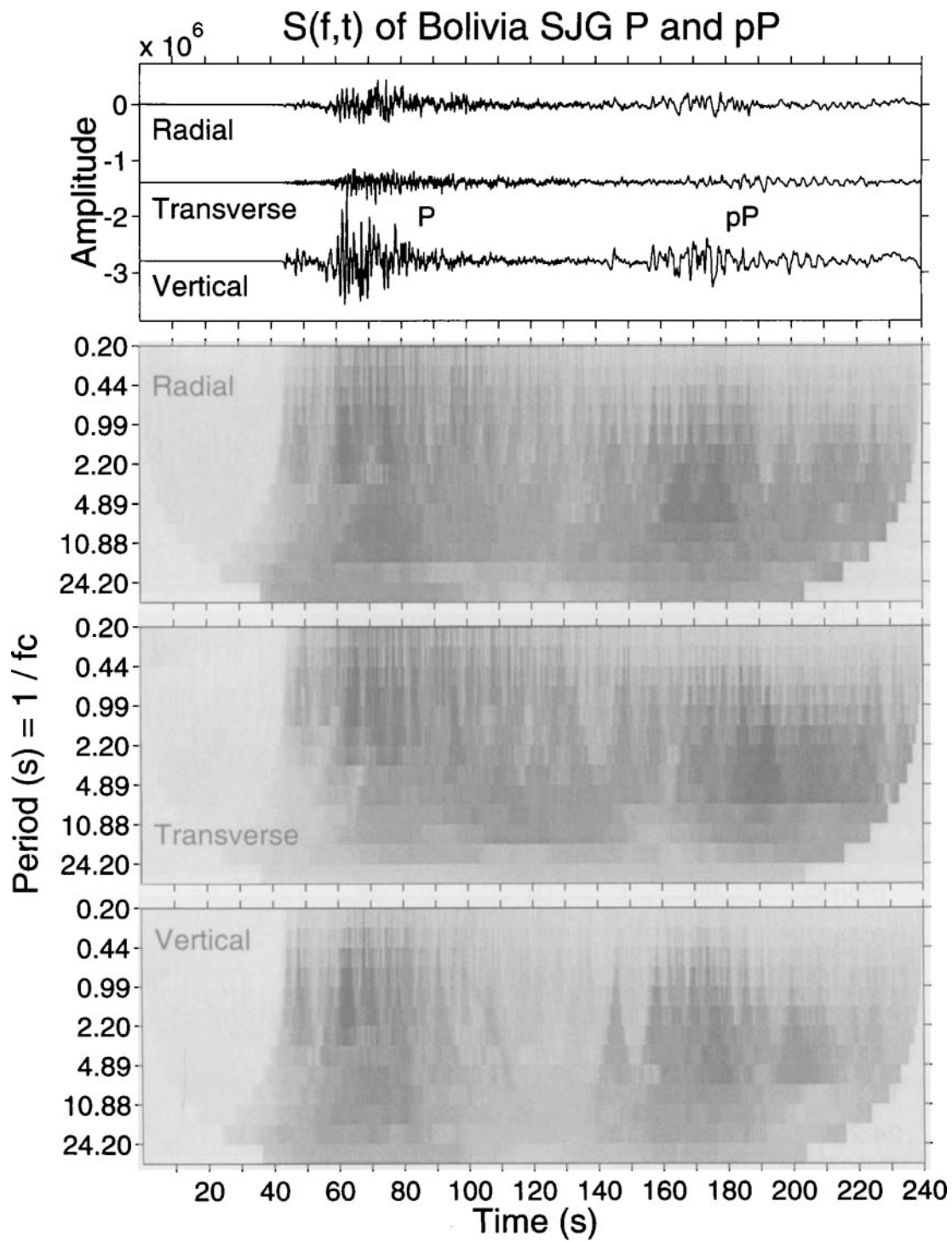


**Figure 12.** Multiwavelet spectral analysis of the broadband  $P$  and  $pP$  phases from the 1994 June 9 deep earthquake beneath northern Bolivia (NEIC magnitude  $m_b = 7.8$ , location  $13.7^\circ\text{S}$ ,  $67.4^\circ\text{W}$ ), recorded at SJG (San Juan, Puerto Rico,  $\Delta = 31.6^\circ$ ). In the same order, the lower panels show the gain-ranged wavelet spectrum estimates for each component of motion. Our analysis uses three complex Slepian wavelets with  $p = 2.5$ ,  $p_c = 3.0$ . Note the deficient spectral amplitude at periods  $2 < T < 5$  s in the  $P$  phase, relative to the  $pP$  phase.

At shorter periods, the secondary polarizations could indicate secondary arrivals. In an expanded image of the  $P$  phase (Fig. 13), the largest area of large  $d_2$  amplitude follows the largest  $d_1$  amplitude by roughly 3 s, consistent with a  $P$ -to- $S$  conversion at the base of a thickened crust

under the island of Puerto Rico. However, the  $d_2$  maximum coincides with a similar maximum in transverse-component energy, so that, on the face of it, the signal indicates a partial  $P$ -to- $SH$  conversion. This seems likely only if conversion occurred at a dipping interface. Alternatively,

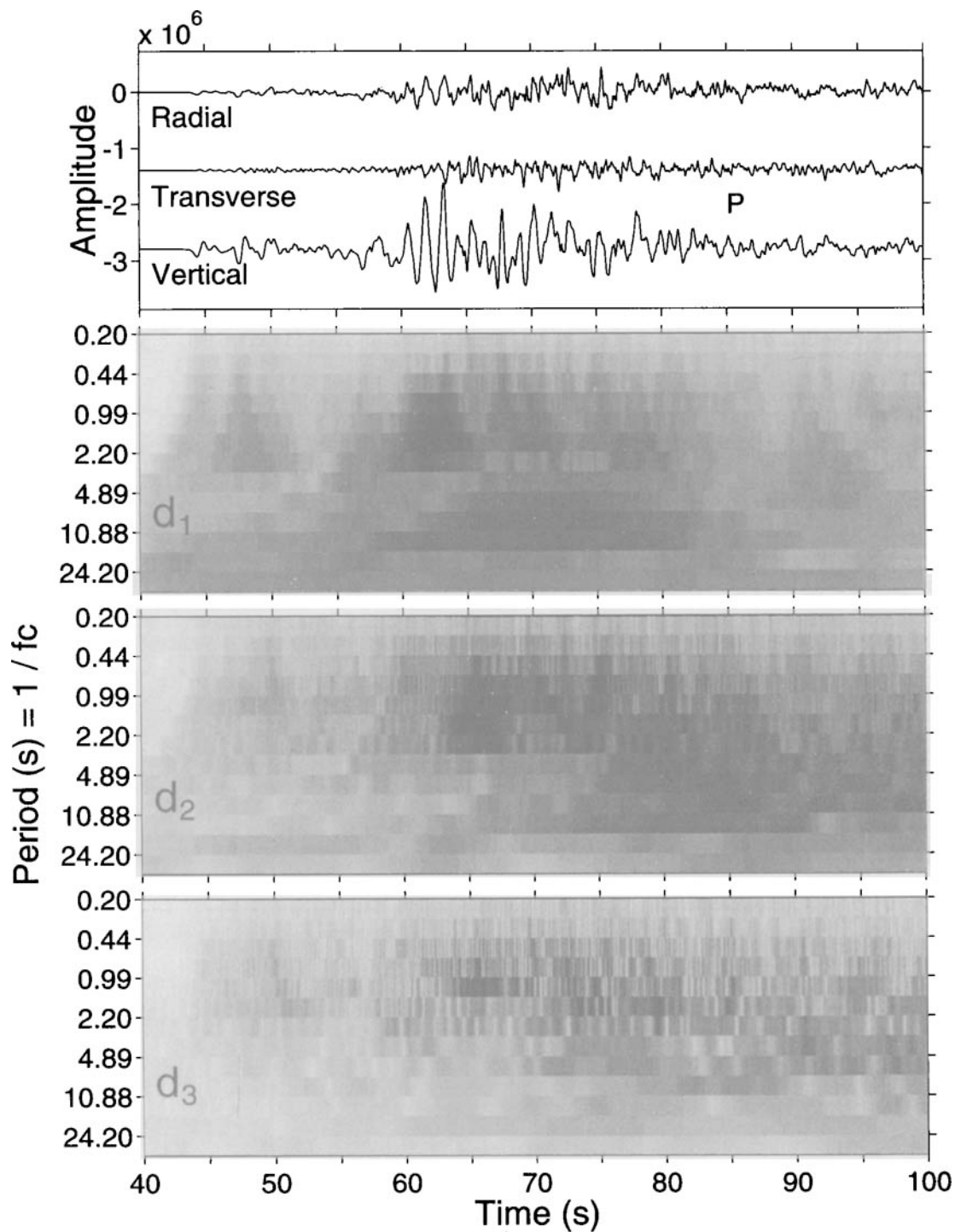


**Figure 13.** Multiwavelet SVD spectra of the  $P$  phase of the 1994 June 9 deep earthquake beneath northern Bolivia, recorded at SJG. The plots magnify the  $P$  time window shown in the previous figure. The  $d_2$  maximum that lags the main  $d_1$  maximum by  $\sim 3$  s coincides with a similar maximum in the multiwavelet spectrum of the transverse-component record, suggesting side-scattered  $P$ , or  $P$ -to- $SH$  forward scattering.

the energy on the transverse component could be a side-scattered  $P$  wave, generated by topography within  $\sim 20$  km of SJG. Similar transverse-component scattered-wave arrivals are seen elsewhere in the Bolivian data set, most notably at ARU (Arti, Russia,  $\Delta = 120.8^\circ$ ), where the scattered wave lags the main  $P$  energy by roughly 13 s.

The polarization of the  $P$  wave is stable and consistent, even within the period range with deficient amplitude (Fig. 14). Polarization analysis reveals a sequence of highly correlated events within the  $P$  phase that correspond to distinct moment releases within the earthquake. The horizontal projection of the correlated particle motion shows

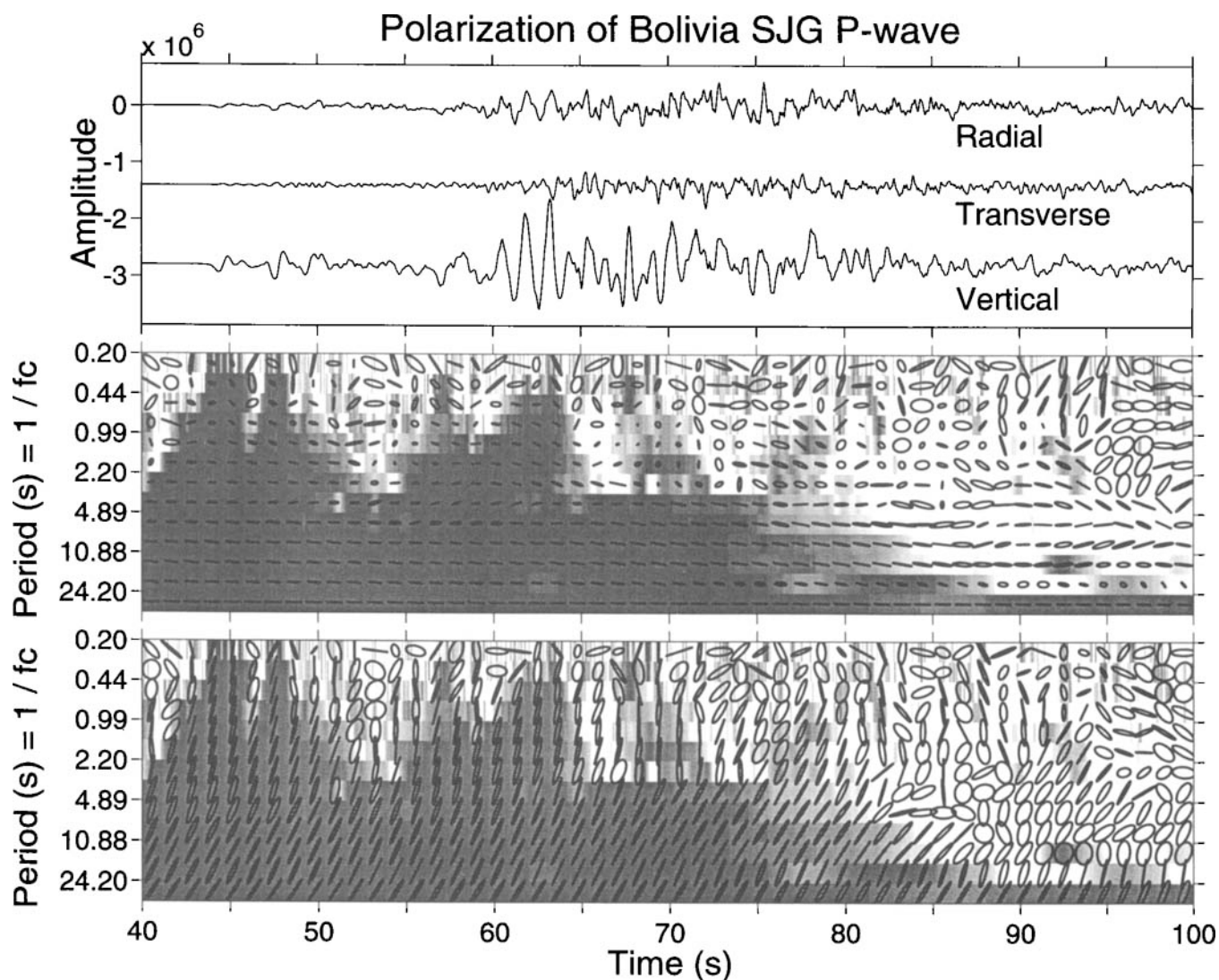


**Figure 14.** Multiwavelet polarization analysis of the broadband  $P$  phase of the 1994 June 9 deep earthquake beneath northern Bolivia, recorded at SJG. Our analysis uses three complex Slepian wavelets with  $p = 2.5$ ,  $p_c = 3.0$ . In the lower panels, the normalized first singular value  $\bar{d}_1$  of the multiwavelet transform matrix  $\mathbf{M}$  is shaded where it exceeds 90 per cent confidence for non-randomness. The central panel shows particle motion in the horizontal plane, with the radial component oriented right-left, and the transverse component oriented up-down. The lower panel shows particle motion in the radial-vertical plane, with the radial component oriented right-left, and the vertical component oriented up-down. Note that coherence weakens in the latter half of this time window, as a result of near-receiver scattering.

that high values of  $\bar{d}_1$  occur where the horizontal motion is small and aligned with the radial component. This makes sense, as the arriving signal is a  $P$  wave at steep-incidence. Where  $\bar{d}_1$  is too small to breach the 90 per cent confidence limit for non-randomness, the horizontal component of the principal polarization vector  $\hat{\mathbf{v}}_1$  is typically much larger, with a larger transverse component. In such cases the polarization vectors shown in Fig. 14 exhibit elliptical motion. This suggests rapid conversion of  $P$  motion to local resonances in the shallow surface layers. We reconstruct the coherent part of the  $P$  wave in Fig 15. In so doing, most of the motion on the transverse component of motion is removed. At 1–2 s periods, however, the coherent motion has a significant projection onto the transverse component.

For three short months in early 1994, the 1994 March 9 earthquake beneath the Fiji Islands (NEIC magnitude

$m_b = 6.4$ , location 17.7°S, 178.6°W, depth  $h = 567$  km) was the largest well-recorded deep earthquake. Wiens *et al.* (1994) report a moment magnitude of  $M_w = 7.6$ . What the Fiji event lacked in size relative to the 1994 June 9 deep Bolivian event was compensated by the relative simplicity of its source time function. This allows a more confident interpretation of the particle motion of individual phases. Fig. 16 shows the wavelet polarization analysis of the  $P$  wavetrain recorded at FFC (Flin Flon, Northwest Territories,  $\Delta = 96.8^\circ$ ). Note the weaker values of  $\bar{d}_1$  for the  $sP$  phase at periods  $T < 2$  s, consistent with higher attenuation during its upper-mantle transit as a shear wave. Note also the tendency for elliptical horizontal motion in the  $PP$  and  $pPP$  phases at  $1 < T < 10$  s, perhaps due to multipathing.

FFC lies within the Canadian Shield, a region of strong upper-mantle anisotropy (Silver & Chan 1991). The SKS

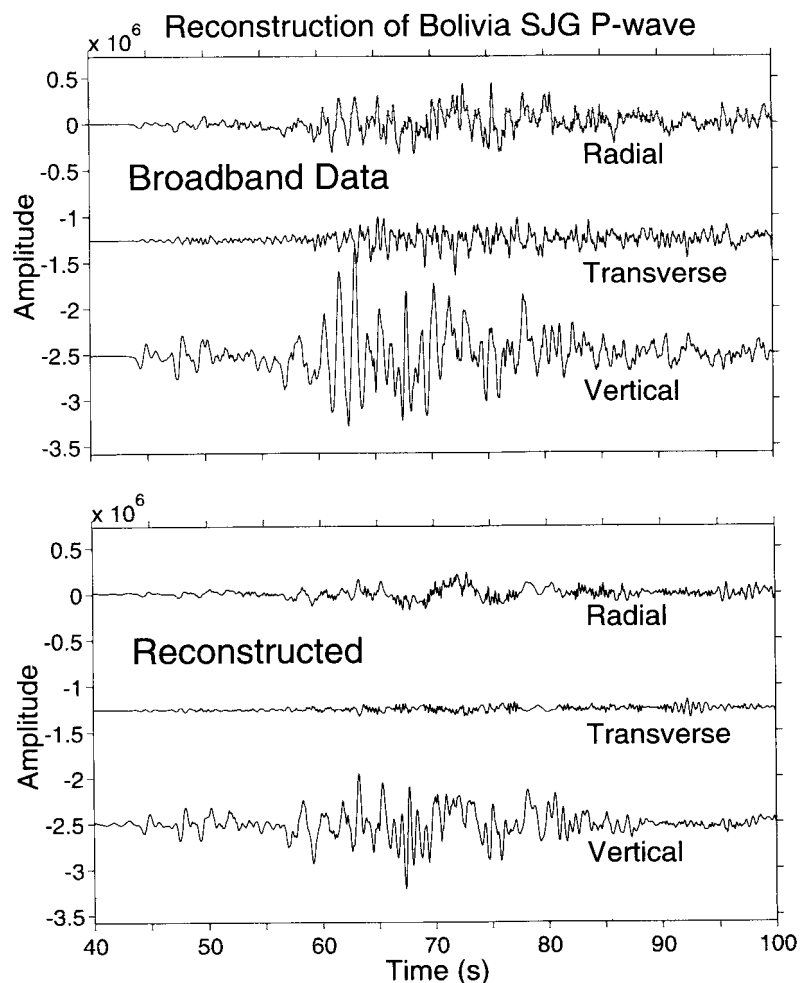


**Figure 15.** Multiwavelet reconstruction of the correlated portion of the  $P$  wave observed at SJG from the 1994 June 9 deep Bolivian event. The reconstruction, a straightforward sum of correlated signal in different passbands, is shown below the data. Note the decreased amplitude of the transverse component of motion.

phase is split into two waves, with particle motion perpendicular and parallel, respectively, to the symmetry axis for anisotropy in the upper mantle beneath the station. The  $SKS$  phase is  $P$ - $SV$  polarized for a spherical-reference isotropic earth model, but splitting caused by anisotropy generates significant motion on the transverse component. If the difference in arrival times between the fast and slow shear waves is small, the transverse-component waveform is roughly proportional to the derivative of the motion on the radial and vertical components. Therefore the horizontal particle motion of a split shear wave is elliptical. This behaviour is clearly expressed in the  $SKS$  wave in the FFC record for periods  $0.5 < T < 15$  s, with ellipticity increasing with decreasing period (Fig. 17). The variable sampling of the time-frequency plane offered by wavelet polarization analysis allows easy identification of a  $P$ -polarized phase  $\sim 10$  s prior to the  $SKS$  phase.

## CONCLUSION

We have adapted a variant of the wavelet transform to the problem of spectral analysis and signal detection with

three-component seismic data. Using frequency-concentration concepts from multiple-taper spectral analysis, we derived a sequence of mutually orthogonal wavelets with optimal spectral leakage properties. We call these discrete functions 'Slepian wavelets'. A family of Slepian wavelet sequences of various lengths  $M$  is parametrized by the dimensionless time-bandwidth and time-bandcentre products,  $p$  and  $p_c$ , respectively, with  $p < p_c$ . For the time-bandwidth product  $p$ , the associated Slepian wavelet family has approximately  $4p - 2$  wavelets with good spectral leakage properties. If  $p \ll p_c$ , the wavelets are frequency-concentrated. If  $p \approx p_c$ , the wavelets are time-concentrated. The most sagacious choice of parameters will depend on the data set analysed. The Slepian wavelets are real-valued, and come in pairs of even and odd functions with similar spectral sampling properties. The pairs can be combined into complex-valued wavelets: the even wavelet as the real part, and the odd wavelet as the imaginary part. This representation has no effect on wavelet spectrum estimates, but enables the estimation of phase lags and leads between different data series.

Multiwavelet spectral analysis convolves a data series with sets of Slepian wavelets to obtain sets of eigenspectra that

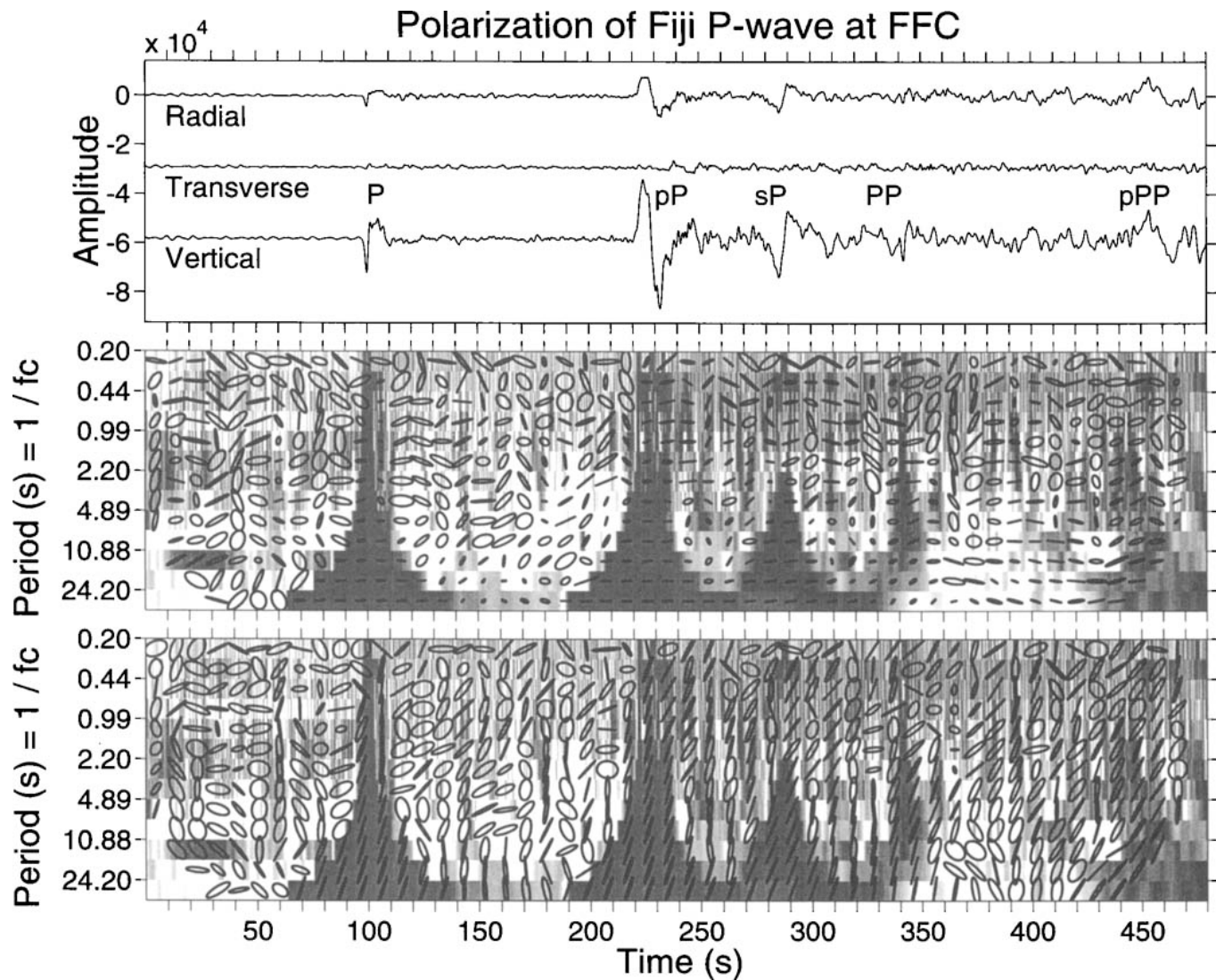


**Figure 16.** Multiwavelet polarization analysis of the broad-band  $P$  wavetrain from the 1994 March 9 deep earthquake beneath the Fiji Islands (NEIC magnitude  $m_b = 6.4$ , location  $17.7^\circ\text{S}$ ,  $178.6^\circ\text{W}$ , depth  $h = 567$  km), recorded at FFC (Flin Flon, Canada,  $\Delta = 96.8^\circ$ ). Our analysis uses three complex Slepian wavelets with  $p = 2.5$ ,  $p_c = 3.0$ . In the lower panels the normalized first singular value  $\bar{d}_1$  of the multiwavelet transform matrix  $\mathbf{M}$  is shaded where it exceeds 90 per cent confidence for non-randomness. The central panel shows particle motion in the horizontal plane, with the radial component oriented right–left, and the transverse component oriented up–down. The lower panel shows particle motion in the radial–vertical plane, with the radial component oriented right–left, and the vertical component oriented up–down.

integrate spectral information in specified areas in the time–frequency plane. The aspect ratio of the time–frequency rectangles varies with the central frequency while retaining a constant area specified by the time–bandwidth product. By comparison, a moving-window discrete Fourier transform, sometimes called an evolutive spectrum estimator, samples the time–frequency plane with a fixed sampling pattern, without adjustment for the period of the signal under investigation. Wavelet eigenspectra from different data series combine into a multiwavelet transform matrix  $\mathbf{M}$ , from which the spectral density matrix estimator  $\hat{\mathbf{S}}(f, t) = (2/K)\mathbf{M}^H\mathbf{M}$  can be calculated, where  $K$  is the number of real-valued Slepian wavelets used. The singular value decomposition (SVD) of  $\mathbf{M}$  identifies correlated variance among the data series, for example components of seismic data at a single observatory. Using results from a

Monte Carlo simulation, we derive empirical confidence limits for the likelihood that a correlated signal among components is not a random noise fluctuation. The first right-singular vector of the multiwavelet transform matrix  $\mathbf{M}$  of three-component seismic motion, identified as the principal polarization, reconstructs the particle motion ellipse as a function of time and frequency. The first left-singular vector defines the pulse shape associated with the principal polarization. We combine information from different rectangles in the time–frequency plane to reconstruct the correlated ‘signal’ in a seismogram. We use a fuzzy-logic criterion that rejects principal polarizations at less than 90 per cent confidence for non-randomness, and increases the weight in the reconstruction as the confidence level increases.

We demonstrate the multiwavelet algorithm with data

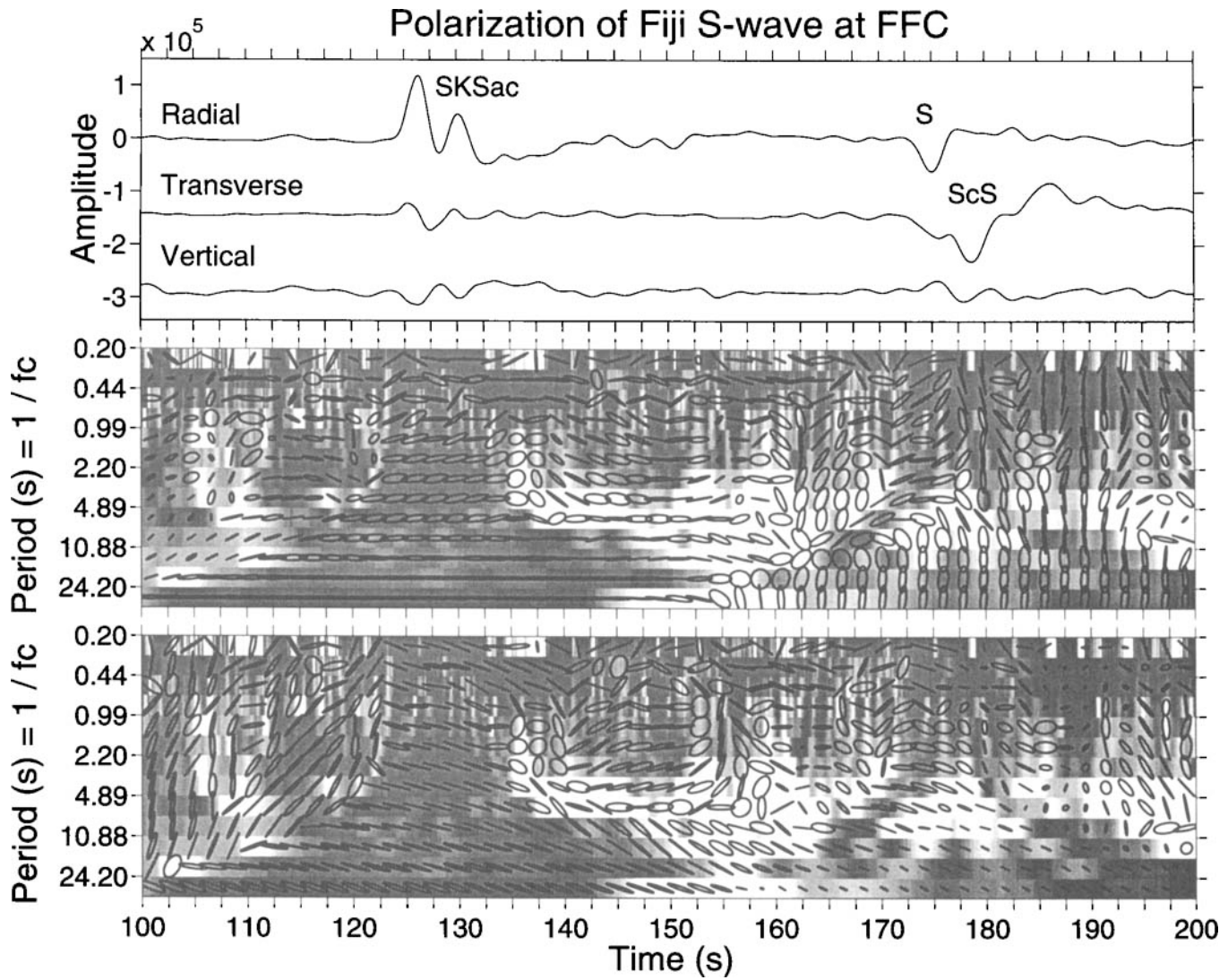


**Figure 17.** Multiwavelet polarization analysis of the broad-band SKS wavetrain of the 1994 March 9 deep Fiji earthquake, recorded at FFC. Our analysis uses three complex Slepian wavelets with  $p = 2.5$ ,  $p_c = 3.0$ . In the lower panels the normalized first singular value  $\bar{a}_1$  of the multiwavelet transform matrix  $\mathbf{M}$  is shaded where it exceeds 90 per cent confidence for non-randomness. The central panel shows particle motion in the horizontal plane, with the radial component oriented right-left, and the transverse component oriented up-down. The lower panel shows particle motion in the radial-vertical plane, with the radial component oriented right-left, and the vertical component oriented up-down. The gradual increase of horizontal ellipticity with decreasing period is consistent with a fixed time shift associated with shear-wave splitting. This pattern breaks down at periods less than 0.75 s, where the signal level is low. A shallow-incidence P phase appears to precede the SKS phase by roughly 10 s.

from three earthquakes. In the first example, wavelet polarization analysis captures successfully the polarization and dispersion behaviour of Love and Rayleigh waves in data from a shallow earthquake. In data from the 1994 June 9 deep Bolivian earthquake, wavelet spectrum estimates identify a spectral ‘hole’ in the P wave, relative to the  $pP$  phase, in the  $3 < T < 5$  s period range, suggesting either unusual scattering or attenuation effects in the deep slab region, or a Doppler effect associated with propagating moment release. In data from the 1994 March 9 deep earthquake beneath the Fiji Islands, wavelet polarization analysis detects a progressive increase in ellipticity between the radial and transverse components of the SKS phase,

consistent with a fixed time delay associated with shear-wave splitting.

#### ACKNOWLEDGMENTS

Helpful discussions with Michael Mann, Yang Yu, Edward Bolton and Huatao Wu are gratefully acknowledged. We thank Greg Wagner for sending us a preprint of his work in bandpassed array processing and signal reconstruction. Seismic data was obtained through the Data Management Center of the Incorporated Research Institutions for Seismology. We thank Project IDA, Project Terrascope and the Albuquerque Seismic Lab of the US Geological Survey

for the quality and rapid accessibility of their data. This work was supported by Air Force Office of Scientific Research contract F49620-94-1-0043.

## REFERENCES

- Beck, S., Silver, P.G., Wallace, T., Myers, S. & James, D., 1994. The rupture properties of the Bolivia earthquake of 1994 from regional portable broadband data I: Seismological observations (abstract), *EOS Trans. Am. geophys. Un.* **465**.
- Daubechies, I., 1992. *Ten Lectures on Wavelets*, SIAM Press, Philadelphia.
- Ekstrom, G., 1994. Teleseismic analysis of the great 1994 Bolivian earthquake (abstract), *EOS Trans. Am. geophys. Un.* **465**.
- Grunbaum, F.A., 1981a. Eigenvectors of a Toeplitz matrix: Discrete versions of the prolate spheroidal wave functions, *SIAM J. Alg. Disc. Meth.*, **2**, 136–141.
- Grunbaum, F.A., 1981b. Toeplitz matrices commuting with tridiagonal matrices, *Linear Algebra and its Applications*, **40**, 25–36.
- Jurkevics, A., 1988. Polarization analysis of three component array data, *Bull. seism. Soc. Am.*, **78**, 1725–1743.
- Kronland-Martinet, R., Morlet, J. & Grossman, A., 1987. Analysis of sound patterns through wavelet transforms, *Int. J. Pattern Recognition and Artificial Intelligence*, **1**, 230–302.
- Lerner-Lam, A.L. & Park, J., 1989. Frequency-dependent refraction and multipathing of 10–100 second surface waves in the western Pacific, *Geophys. Res. Lett.*, **16**, 527–530.
- Mann, M. & Park, J., 1994. Global-scale modes of surface temperature variability on interannual to century timescales. *J. geophys. Res.*, **99**, 25 819–25 833.
- Okal, E.A., Engdahl, E.R., Kirby, S.H. & Huang, W.-C., 1994. Deep South American earthquakes: The general context of the large 09 June 1994 Bolivian shock, an extraordinary event in an extraordinary Wadati-Benioff zone (abstract), *EOS Trans. Am. geophys. Un.*, **465**.
- Park, J., Lindberg, C.R. & Vernon III, F.L., 1987a. Multitaper spectral analysis of high-frequency seismograms, *J. geophys. Res.*, **92**, 12 675–12 684.
- Park, J., Vernon III, F.L., & Lindberg, C.R., 1987b. Frequency-dependent polarization of high-frequency seismograms, *J. geophys. Res.*, **92**, 12 664–12 674.
- Percival, D.B., & Walden, A.T., 1993. *Spectral Analysis for Physical Applications*, Cambridge University Press, Cambridge.
- Press, W.H., Teukolsky, S.A., Vetterling, W.T. & Flannery, B.P., 1992. *Numerical Recipes in FORTRAN*, 2nd edn, Cambridge University Press, Cambridge.
- Silver, P.G., & Chan, W.W., 1991. Shear-wave splitting and subcontinental mantle deformation, *J. geophys. Res.*, **96**, 16 429–16 454.
- Slepian, D., 1978. Prolate spheroidal wave functions, Fourier analysis, and uncertainty—V: The discrete case, *Bell System Tech. J.*, **57**, 1371–1430.
- Slepian, D., 1983. Some comments on Fourier analysis, uncertainty and modeling, *SIAM Review*, **24**, 379–393.
- Thomson, D.J., 1982. Spectral estimation and harmonic analysis, *IEEE Proc.*, **70**, 1055–1096.
- Thomson, D.J., 1990. Time series analysis of Holocene climate data, *Phil. Trans. R. Soc. Lond.*, **330**, 601–616.
- Vernon, F.L., Fletcher, J., Carroll, L., Chave, A. & Sembrera, E., 1991. Coherence of seismic body waves from local events as measured by a small-aperture array, *J. geophys. Res.*, **96**, 11 981–11 996.
- Vidale, J.E., 1986. Complex polarization analysis of particle motion, *Bull. seism. Soc. Am.*, **76**, 1393–1405.
- Wagner, G.S. & Owens, T.J., 1993. Broadband bearing-time records of three-component seismic array data and their application to the study of local earthquake coda, *Geophys. Res. Lett.*, **20**, 1823–1826.
- Wagner, G.S. & Owens, T.J., 1995. Broadband eigen-analysis for three-component seismic array data, *Geophys. J. Int.*, in press.
- Wiens, D.A., McGuire, J.J., Shore, P.J., Bevis, M.G., Draunidalo, K., Prasad, G. & Helu, S.P., 1994. Aftershocks of the March 9, 1994 Tonga event: The strongest aftershock sequence of a deep earthquake (abstract), *EOS Trans. Am. geophys. Un.*, **466**.

## APPENDIX: SLEPIAN WAVELETS WITH THE MATLAB PACKAGE

All calculations in this paper were performed using the commercially available Matlab software package on a Sparc 10 workstation. Although this package (and others like it) does not always offer the fastest method to perform certain applied mathematics operations (e.g. specialized eigenvector decompositions), it was very helpful in algorithm development. For the reader interested in using Slepian wavelets, we present a Matlab M-file to calculate  $n_{win} = 6$  real-valued 100 point wavelets for the time–bandwidth product  $p = 2.5$ , and the time–bandcentre product  $p_c = 5$ . The wavelets are output in an array named `tap`.

```
n=100; nwin=6; p=2.5; pc=5.0
% first calc the Toeplitz matrix row
fw=p/n; fo=pc/n;
x=linspace(2*pi, (n-1)*2*pi, n-1);
sink1=2.0*sin((fo+fw)*x)./x;
sink1=[2.0*(fo+fw) sink1];
sink2=2.0*sin((fo-fw)*x)./x;
sink2=[2.0*(fo-fw) sink2];
sink=sink1-sink2;
slep=teoplitz(sink);
[V, D]=eig(slep);
% eigenvalues are not ordered by matlab
% function, so we sort them
[eigv, k]=sort(diag(D)); V=V(:, k);
% reorder last nwin eigenvectors and eigenvalues
% to first lambda=eigv(n:-1:n-nwin+1);
tap=V(:, n:-1:n+1-nwin);
% set sign convention for wavelets
for k=1:nwin
    if(tap(2, k)<0)
        tap(:, k)=-tap(:, k);
    end
end
```

We calculated the wavelet transform of a data set with the Matlab `conv` function. This evaluates the wavelet transform at many more points than is perhaps necessary for the longer wavelets.